Surv Geophys (2007) 28:121–167
DOI 10.1007/s10712-007-9019-6

ORIGINAL PAPER

MT+, Integrating Magnetotellurics to Determine Earth Structure, Physical State, and Processes

Paul A. Bedrosian

Received: 19 December 2006 / Accepted: 1 June 2007 / Published online: 6 July 2007

Abstract As one of the few deep-earth imaging techniques, magnetotellurics provides information on both the structure and physical state of the crust and upper mantle. Magnetotellurics is sensitive to electrical conductivity, which varies within the earth by many orders of magnitude and is modified by a range of earth processes. As with all geophysical techniques, magnetotellurics has a non-unique inverse problem and has limitations in resolution and sensitivity. As such, an integrated approach, either via the joint interpretation of independent geophysical models, or through the simultaneous inversion of independent data sets is valuable, and at times essential to an accurate interpretation. Magnetotelluric data and models are increasingly integrated with geological, geophysical and geochemical information. This review considers recent studies that illustrate the ways in which such information is combined, from qualitative comparisons to statistical correlation studies to multi-property inversions. Also emphasized are the range of problems addressed by these integrated approaches, and their value in elucidating earth structure, physical state, and processes.

Keywords Magnetotellurics · Integrated interpretation · Inverse problems · Cooperative inversion

1 Introduction

This review focuses on the interpretation of magnetotelluric (MT) data in combination with independent geophysical, geological, and geochemical data. An integrated interpretation is a value-added approach, in which the integration process itself leads to a greater understanding. Integration is fundamentally a combining of information; in this review I do not

18th IAGA WG 1.2 Workshop on Electromagnetic Induction in the Earth. El Vendrell, Spain, September 17–23, 2006.

P. A. Bedrosian (✉)
CICT, US Geological Survey, Denver Federal Center, MS 964, Denver, CO 80225, USA
e-mail: pbedrosian@usgs.gov

focus on the sources of information, but rather on the types of questions addressed and the ways in which information is combined. As this review concerns magnetotellurics, the examples considered are aimed at crustal and upper-mantle scales. Many of the approaches described, however, apply equally well to shallow electromagnetic methods, or more generally to any geophysical method with a non-unique inverse problem. In the studies presented, the pertinent questions center upon the structure and geometry of the subsurface, the physical, thermal, and compositional state of earth materials, and dynamic earth processes including faulting, orogenesis, subduction, and rifting. By way of introduction, I begin by discussing magnetotelluric imaging and model assessment, conductivity mechanisms, sources of lithospheric conductivity, and the advantages of an integrated interpretation.

1.1 Magnetotelluric Imaging

The determination of subsurface conductivity (or its inverse, resistivity) at crustal scales is the domain of magnetotellurics, a natural-source electromagnetic technique which involves surface measurements of orthogonal electric and magnetic field variations (Tikhonov 1950; Caignard 1953). The natural electromagnetic signals used in magnetotellurics originate from a variety of processes in the atmosphere, ionosphere, and magnetosphere. Within the typical magnetotelluric frequency range (10^4 to 10^{-4} Hz), signal above 1 Hz is largely due to electrical storms in the atmosphere, while signal below 1 Hz is dominantly the result of plasma waves within the ionosphere and magnetosphere (Vozoff 1991). Due to the strong conductivity contrast at the air-earth boundary, the inducing electromagnetic fields, regardless of incidence angle, are strongly refracted, and propagate vertically within the earth. Relative to the incident magnetic field, the amplitude and phase of the measured electric field depend upon the conductivity of the medium it travels through. At magnetotelluric frequencies, the propagation of electromagnetic energy in the earth is described by a diffusion equation, of the same form as that governing heat diffusion through a solid.[1] The solutions to this equation are electric and magnetic fields which decay exponentially within the earth over a characteristic distance, δ, termed the skin depth. Over a homogeneous earth, the skin depth is related to the frequency ($\omega = 2\pi f$) of the incident field and the resistivity (ρ) of the subsurface by

$$\delta = \sqrt{2\rho/\mu\omega} \approx 500\sqrt{\rho/f} \ \text{ meters}, \tag{1}$$

where μ is magnetic permeability, typically assumed equal to its free space value, μ_o. Equation 1 is a statement of penetration depth, with lower frequencies penetrating deeper within the earth and averaging over an increasing earth volume. For a typical survey, the depth of investigation is additionally dependent upon sampling rate, recording time, signal strength, site density, and profile length. Magnetotellurics is the only geophysical technique capable of *imaging* electrical resistivity structure from the near surface through to the upper mantle. An imaging technique (also referred to as a sounding method) is one in which the measured geophysical data at a single location have differing depth sensitivity.

[1] Wave-propagation techniques, such as ground-penetrating radar, operate at higher frequencies (100 MHz–1 GHz), have better spatial resolution than magnetotellurics, but are very limited in depth penetration ($\leq$50 m).

In seismic imaging, for example, travel time is the variable that separate data of differing depth sensitivity. In the case of magnetotellurics, it is frequency.

The goal of magnetotelluric analysis is to estimate the earth's heterogeneous and sometimes anisotropic resistivity structure from surface field measurements. The measured fields are typically transformed to the frequency domain where cross- and auto-power spectra are computed. These are then used to estimate transfer functions relating the frequency-domain fields:

$$\begin{bmatrix} E_x \\ E_y \end{bmatrix} = \begin{bmatrix} Z_{xx} & Z_{xy} \\ Z_{yx} & Z_{yy} \end{bmatrix} \begin{bmatrix} H_x \\ H_y \end{bmatrix}. \tag{2}$$

In Eq. 2, the four elements Z_{ij} form the impedance tensor, a complex, frequency-dependent tensor containing the amplitude and phase relations between $2E(\omega)$ and $2H(\omega)$. From each element of the impedance tensor can be derived the magnetotelluric response functions, apparent resistivity (ρ_a) and phase (φ) defined as

$$\rho_{a,ij}(\omega) = \frac{1}{\mu\omega}\left|Z_{ij}(\omega)\right|^2 \quad \text{and} \quad \varphi_{ij}(\omega) = \tan^{-1}[\Im(Z_{ij}(\omega))/\Re(Z_{ij}(\omega))]. \tag{3}$$

The form of the impedance tensor, $2Z(\omega)$, is related to the dimensionality of the electromagnetic field, which in turn reflects the complexity of the subsurface conductivity distribution.[2] In the case of layer-cake structure (1D), where conductivity varies only with depth, the impedance tensor reduces to

$$\overleftrightarrow{Z}_{1D}(\omega) = \begin{bmatrix} 0 & Z \\ -Z & 0 \end{bmatrix}. \tag{4}$$

In the special case of a homogeneous earth, the impedance tensor, and therefore the magnetotelluric response functions, is frequency independent. The apparent resistivity, ρ_a, is identical to the subsurface resistivity, ρ, while the phase, ϕ, is equal to 45°. For more complicated structure, the resistivity distribution is folded into the frequency dependence of the impedance tensor, and is extracted via modeling and inversion.

For the case of two-dimensional (2D) earth structure, where conductivity varies with depth and in one lateral direction, the impedance tensor takes the form

$$\overleftrightarrow{Z}_{2D}(\omega) = \begin{bmatrix} 0 & Z_{xy} \\ Z_{yx} & 0 \end{bmatrix}, \tag{5}$$

when rotated into a coordinate system parallel to geo-electric strike (the direction of uniform conductivity). These reduced forms of the impedance tensor (Eqs. 4, 5) are of special significance as they permit simplification of the inversion process used to convert frequency-dependent apparent resistivity and phase into depth-dependent resistivity. In the case of three-dimensional (3D) earth structure, the impedance tensor is fully occupied. This fully-occupied form may also arise from intrinsic electrical anisotropy (direction-dependent conductivity) in a structurally 2D subsurface.

[2] The converse is not necessarily true. For example, along a symmetry axis of a three-dimensional conductivity distribution, the electromagnetic field, and hence the impedance tensor, may exhibit a lower dimensionality.

The magnetotelluric inverse problem is non-linear in its relation between data (apparent resistivity and phase at a number of frequencies and a number of sites) and model parameters (resistivity at a set of subsurface cells or nodes). By linearizing the forward problem,[3] an iterative inversion is employed in which a data misfit functional (ϕ_d) of the form

$$\phi_d = (\vec{d} - \vec{F}[\vec{m}_i])^T \vec{C}_d^{-1} (\vec{d} - \vec{F}[\vec{m}_i]) \tag{6}$$

is minimized, where $\boldsymbol{d}$ is the data vector, $\boldsymbol{m}$ is the model vector, $2C_d$ is the diagonal data covariance matrix containing the data errors, and $\boldsymbol{F[m]}$ denotes the linearized forward response of model $\boldsymbol{m}$ (Eq. 7), i.e., the data that would be measured if subsurface conductivity were given by model $\boldsymbol{m}$.

$$\vec{F}[\vec{m}_{i+1}] = \vec{F}[\vec{m}_i] + \left(\partial \vec{F} / \partial \vec{m}_i\right) \delta \vec{m}_i \tag{7}$$

Though in principle Eq. 6 will converge to a unique solution ($\phi_d = 0$), in practice the magnetotelluric inverse problem is non-unique due to data errors, spatially under-sampled data, a limited frequency band, model parameterization, and physical assumptions regarding dimensionality (Parker 1980). For this reason the inversion is typically regularized by placing additional constraints on the solution (Tikhonov and Arsenin 1979). The inversion thus seeks to minimize an expanded functional (ϕ) of the form

$$\phi = \phi_d + \lambda \phi_m, \quad \text{where} \quad \phi_m = (\vec{m} - \vec{m}_o)^T \vec{C}_m^{-1} (\vec{m} - \vec{m}_o). \tag{8}$$

Regularization is achieved through the model structure functional, ϕ_m, defined by a model covariance matrix, $2C_m$, used to characterize the spatial continuity of the resistivity model, $\boldsymbol{m}$, relative to a prior model, $2m_o$. The matrix $2C_m$ can be viewed as a discrete model-structure operator, and is commonly used either to enforce similarity to the prior model (Marquardt 1970) or to produce a smooth, minimum-structure ($\nabla^2 m$) model (de Groot-Hedlin and Constable 1990; Rodi and Mackie 2001). The relative importance of ϕ_d and ϕ_m during inversion is controlled by λ, a trade-off parameter. More information on geophysical inverse theory and the magnetotelluric inverse problem may be found in Aster et al. (2005), Scales et al. (2001), Parker (1994), and Menke (1984).

Goodness of fit is evaluated using a normalized χ^2 statistic, with a misfit of one indicating an ideal fit (Bevington and Robinson 1992). A low misfit, however, should be viewed as a necessary but insufficient condition for determining the validity of an inverse model. Rigorous model assessment, as discussed next, must further be applied. A more detailed description of the magnetotelluric method and its development can be found in Simpson and Bahr (2005), Jiracek et al. (1995), Jones (1992), and Vozoff (1991).

1.2 Model Assessment

Model non-uniqueness necessitates an exploration of the subspace of models consistent with the data. Given N data and M model parameters, an N × M Jacobian matrix is

[3] The forward problem involves calculating the surface electric and magnetic fields expected for a given subsurface conductivity distribution.

computed when linearizing the forward problem ($\partial\vec{F}/\partial\vec{m}_i$ in Eq. 7). This matrix is termed the sensitivity matrix, and relates linear perturbations of the M model parameters to the N data. The resolution of individual mode cell resistivities is defined by diagonal values of the resolution matrix, formed from singular-value decomposition (SVD) (Lanczos 1997) of the sensitivity matrix (Menke 1984). This calculation, however, is computationally intensive and rarely performed. A nullspace projection approach, based on a truncated SVD, is more accessible, and can be used to examine a range of alternate models consistent with the data (Muñoz and Rath 2006). A relatively simple approach is to examine normalized columnwise sums of the sensitivity matrix, which represent the average sensitivity of a given cell resistivity to all data (Schwalenberg et al. 2002). It must be stressed, however, that all of the above methods are examples of linear sensitivity analysis, and are only valid in assessing the sensitivity of an inverse model to small perturbations from the original model.

An exhaustive probabilistic approach can be applied to examine the model space, including large perturbations from the inverse model (Mosegaard and Tarantola 2002; Mosegaard and Sambridge 2002). This approach, however, is computationally prohibitive, and in practice a combination of forward modeling and constrained inversion are used to investigate alternate models. This is generally a trial-and-error process in which the geometry or conductivity of parts of a model are altered.[4] Both forward modeling and constrained inversion tend to be hypothesis driven, and seek to determine whether alternate model structures are permissible. In forward modeling, the forward response of the altered model is calculated and the resulting data misfit compared to the misfit of the unaltered model (Nolasco et al. 1998). A misfit equal to (less than) that of the unaltered model implies that the modified model is an equal (a better) solution. An increased misfit cannot be directly interpreted unless constrained inversion is performed, as alternate models with differing structure outside the region of modification may provide an equivalent solution, but are not tested through the forward modeling approach.

Constrained inversion refers to an inversion in which constraints are applied regionally, either to test a hypothesis or to include independent a priori information in the inversion process. Constrained inversions are carried out within a regularized inversion scheme, the distinction being the addition of one or more localized constraints.[5] Constrained inversions can be classified according to the form of constraint applied. Hard constraints include fixing model parameters or their gradients within the model. Soft constraints, in contrast, include localized changes in model regularization (e.g., relaxing the smoothing regularization in a region) or the enforcement of spatial statistics. Soft constraints do not explicitly specify conductivity structure, but rather steer the inversion toward models consistent with the given criterion. This topic is considered in more detail in the discussion section.

The results of a constrained inversion help define the range of permissible models. For example, to test the necessity of a conductive model feature, it could be replaced by the background resistivity and the region fixed to prohibit modification. An inversion starting from this modified model will then either converge with a misfit similar to the original model, or will result in a higher misfit. The former suggests an alternate model consistent with the data, while the latter indicates the modification (constraint) is incompatible with the data.

Global assessment is another important part of model assessment. The relative importance of model regularization and data misfit is controlled by λ, the trade-off parameter

[4] An automated, random structure modification algorithm has been suggested by Muñoz and Rath (2006).

[5] Regularization is itself a constraint on the inversion, though it is global rather than localized in its extent.

(Eq. 8). Upon running a suite of inversions with different values of λ, a plot of data misfit (ϕ_d) vs. model structure (ϕ_m) defines an L-shaped curve. It is the 'knee' of this so-called L-curve, which defines an optimum trade-off between data misfit and regularization (Parker 1994). Global assessment also includes examining how variations in the type of regularization, the model mesh, the choice of starting model, or the inclusion/exclusion of certain data affect the resulting inverse model. In examining the resulting suite of models, robust model features can be identified, and their range in resistivity and geometry gives an indication of the range of permissible structures.

A final aspect of model assessment concerns spatial resolution. In magnetotellurics, spatial resolution is not a purely geometric effect (station layout, frequency range, model parameterization) but is strongly model-dependent. Two measures of spatial resolution are considered: what is the minimum-size structure that can be resolved, and with what accuracy can a resistivity boundary be recovered?

In seismic refraction studies, checkerboard tests (Zelt 1998) are employed to determine the minimum resolvable structure. In such tests, a checkered grid of velocity perturbations is used as the starting model for a synthetic inversion using the same survey geometry and model discretization as for the field data inversion. The extent to which this checkered structure is recovered in the inverse model gives an indication of spatial resolution in various parts of the velocity model. Such methods are of limited utility in magnetotellurics, however, due to the strong non-linearity between subsurface resistivity and the amplitude of the surface electromagnetic fields. Relative to a background resistivity, a negative resistivity perturbation (more conductive) decreases the resolution of underlying structure, while a positive perturbation (less conductive) can enhance the resolution of underlying structure. This so-called screening effect will be illustrated in a later section.

Resolution is best expressed as a percent of electrical skin depth, which for layered-earth structure is proportional to the square root of resistivity (Orange 1989). In comparing layers of resistivity ρ_1 and ρ_2, with $\rho_2 > \rho_1$, the minimum resolvable thickness of the resistive layer is equal to $\sqrt{\rho_2/\rho_1}$ times that of the conductive layer. Simply put, thin conductive layers are more easily resolved than thin resistive layers. Additionally, as with all geophysical methods, the spatial resolution of magnetotellurics changes with depth. Thus the minimum resolvable thickness of a near-surface layer will become significantly larger if the layer is deeply buried.

The resolution of resistivity boundaries is direction dependent. As a rule of thumb, magnetotellurics has a lateral resolution similar to reflection seismology and a vertical resolution comparable to seismic refraction (Jones 1987). The excellent lateral resolution arises from the predominantly horizontal current flow induced by the source fields, resulting in a discontinuous electric field across a lateral resistivity boundary. The vertical resolution of a boundary, in contrast, is strongly influenced by the overlying model conductivity. For a layered-earth model, resolution of the depth to resistive basement is on the order of 10% of depth (Orange 1989).

1.3 Conductivity Mechanisms

Bulk electrical resistivity, and its inverse, conductivity, range over 10 orders of magnitude for earth materials (Guéguen and Palciauskas 1994; Palacky 1987; Haak and Hutton 1986; Keller, 1987). For (non-marine) magnetotelluric surveys, crustal resistivity typically spans 3–4 orders of magnitude. Resistivity thus has a wide 'dynamic range' in comparison to seismic velocities which vary by a factor of 10, or rock densities which vary by a factor of

3 (Guéguen and Palciauskas 1994). On average, the upper crust is quite resistive ($\sim 10^4$ Ω m), reflecting the low conductivity of most silicate and carbonate rocks (Gough, 1986). In contrast, the lower continental crust is more conductive (20–30 Ω m), likely due to the presence of a minor conducting phase (Hyndman and Shearer 1989; Haak and Hutton 1986; Shankland and Ander 1983). Mantle conductivity mimics that of the crust, with a relatively resistive (though largely unconstrained) upper mantle underlain by a conductive asthenosphere (Jones 1999). In comparison to the continents, oceanic lithosphere is quite homogeneous, with average resistivities on the order of 1000 Ω m below the first 100–200 m which typically fall within the range of 1–10 Ω m. Typical oceanic upper mantle is characterized by resistivities of $\sim 10^4$ Ω m.

Lithospheric magnetotelluric studies seek physical explanations for regions of anomalous conductivity, i.e., deviations from the general structure described above. As alluded to previously, the presence of a minor conducting phase can dramatically increase bulk conductivity. Certain mineralogies, such as metallic sulfides and graphite, are highly conductive ($\sigma \geq 100$ S/m) and can give rise to enhanced conductivity when present in small percentages provided they are well connected (Nover et al. 2005; Ádám 2005; Raab et al. 1998; Jödicke 1992). The formation of graphite from organic carbon requires extreme temperatures (>1000°C) unless strain energy is present which can catalyze graphitization at mid-crustal conditions (>450°C) (Ross and Bustin 1990; Nover et al. 2005). Graphite observed in the deeper levels of fold and thrust belts, as well as in sutures and fossil shear zones, is assumed to have formed under these conditions. In addition to metamorphic graphite, fluid-deposited graphite may occur in volcanic terranes, and is commonly precipitated from hot (>600°C) magmatic fluids (Luque et al. 1998).

Sulfides and graphite tend to be either stratigraphically bound (depositional source) or limited in their areal extent (tectonic or magmatic origin). In deep basin strata, they are sometimes found together, where anoxic conditions can lead to large-scale deposition of organic carbon and sulfides from blue-green algae hosting sulfate-reducing bacteria. Sulfides and graphite can often be identified from the surrounding geology and confirmed using geophysical techniques such as magnetic surveying and induced polarization (Telford et al. 1976). The expansive conductivity anomalies observed within *active* tectonic margins are rarely due solely to these minerals.

Aqueous fluids and partial melt are the most common causes of large-scale conductivity anomalies within active tectonic regimes (Hyndman and Hyndman 1968; Wei et al. 2001; Li et al. 2003). In both cases, rock conductivity is dominated by ionic conduction within the fluid phase. In the case of aqueous fluids, conductivity is strongly dependent upon fluid salinity, temperature, porosity, the interconnectivity of the fluid phase, and to a lesser degree pressure. The conductivity of partial melt is likewise dependent on temperature, interconnectivity, and pressure, but additionally varies with the amount of water (both free and structurally bound) and oxygen fugacity (Waff and Weill 1975). Aqueous fluids and partial melt are involved in a range of tectonic processes. Their range of stability is largely determined by temperature and pressure (roughly linear with depth), and also to an extent by composition and tectonic setting.

Neglecting compositional differences, the onset of dry melting requires temperatures of about 1200°C, while water-saturated rocks begin to melt around 650°C (Lebedev and Khitarov 1964). Water-undersaturated melting spans this temperature range and is the most likely scenario for lower-crustal melting.[6] The conductivity of the melt phase varies

[6] The calculated pre-eruptive water content of silicic magmas is on the order of 2.5–6.5 wt%, suggesting they originate at depth in water-undersaturated melt conditions (Burnham 1997).

slightly with rock composition, but typically falls within the range of 1–10 S/m (Tyburczy and Waff 1983). In contrast to both dry and water-saturated melt, which exhibit an increase of melt conductivity with temperature, water-undersaturated melts show a decrease in conductivity with increased temperature, attributed to dilution of water into the melt phase (Wannamaker 1986).

The bulk conductivity of partially molten rock depends not only on the melt conductivity, but also on its distribution within the supporting rock matrix. Partial melt can be treated as a two-phase system, and effective medium theory used to bracket a permissible range of melt fractions given magnetotelluric estimates of bulk conductivity (Hashin and Shtrikman 1962). The so-called Hashin–Shtrikman upper and lower bounds correspond to the upper and lower limits of bulk conductivity (σ_B) when the melt and rock matrix are connected in parallel and in series, respectively:

$$\sigma_U = \sigma_1 + \frac{f_2}{\frac{1}{\sigma_2 - \sigma_1} + \frac{f_1}{3\sigma_1}} \geq \sigma_B \geq \sigma_2 + \frac{f_1}{\frac{1}{\sigma_1 + \sigma_2} + \frac{2_1}{3\sigma_2}} = \sigma_L. \tag{9}$$

In the above, f_1 and f_2 are the volume fractions, and σ_1 and σ_2 the conductivities, of the pure melt and rock matrix, respectively. Numerous mixing models exist, however, it is difficult to attain bulk conductivities in excess of 1 S/m at lower-crustal pressures and temperatures unless water-saturated melt fractions exceed 30% (Li et al. 2003). Assuming water-undersaturated melts, bulk conductivity is rarely expected to exceed 0.1 S/m (Wannamaker 1986).

As with partial melt, the distribution of aqueous fluids within a rock matrix strongly affects bulk conductivity. The empirically-derived Archie's Law (Archie 1942) relates bulk resistivity (ρ_B) to porosity (ϕ), fluid resistivity (ρ_F), pore saturation (S), and pore geometry via

$$\rho_B = \rho_F \varphi^{-m} S^{-n}, \tag{10}$$

where m is an exponent controlling pore geometry and typically ranges between 1 (crack-like pores) and 2 (spherical pores). The saturation exponent n is constant for a given fluid-rock system. A modified Archie's Law has been formulated for partial melt, relating melt fraction to bulk conductivity, and gives values intermediate to the Hashin–Shtrikman bounds (Hermance 1979).

For aqueous fluids, the conductivity of the fluid phase depends on temperature, pressure, and the ionic species present and their concentrations. For salt solutions, fluid conductivity generally increases as a function of concentration, however at very high concentrations (30–40 wt%) begins to decrease, and ultimately approaches the conductivity of the molten salt. The particular salt matters to some extent, with differing mobilities resulting in an approximately one order of magnitude difference in fluid conductivity (Guéguen and Palciauskas 1994). At a fixed concentration and (upper-crustal) pressure, fluid conductivity increases with temperature until 300–400°C due to increased ionic mobility caused by the decreasing viscosity of water. Beyond these temperatures, conductivity begins to fall as a result of increased ion association. As the onset of wet partial melting occurs around 650°C this is likely the highest equilibrium temperature at which free aqueous fluids can exist. Fluid conductivity is independent of pressure at lower temperatures (up to $\sim$300°C), and increases with pressure at higher temperatures (Quist and Marshall 1968). These data can be combined to estimate expected fluid conductivities at upper- and mid-crustal conditions which generally fall in the range of 1–30 S/m, with an extreme value of 100 S/m for hypersaline brines (e.g., 25 wt% NaCl).

Although the simplest picture of aqueous crustal fluids involves only chloride salts, dissolved CO_2 may also contribute to fluid conductivity within the ductile lower-crust. When pore fluids approach lithostatic pressure, CO_2 can be present at concentrations approaching 20 mol%, and react with H_2O to form H_2CO_3 (Nesbitt 1993). Dissociation reactions lead to the formation of HCO_3^- in concentrations large enough to increase fluid conductivity by several orders of magnitude (Nesbitt 1993). Thus, if fluids are present within the lower crust, enhanced fluid conductivity may arise from the additional presence of bicarbonate salts.

1.4 Deep-crustal Conductivity

Much of the research into sources of enhanced conductivity (and their fields of stability) stems from observations of high conductivity within the continental lower crust (Hyndman and Shearer 1989; Haak and Hutton 1986; Shankland and Ander 1983). Laboratory measurements, however, on lower-crustal rocks at representative pressure and temperature conditions yield low conductivities (Kariya and Shankland 1983), thus sparking a lively debate as to the origins of lower-crustal conductivity. Within active tectonic regimes, the explanation of conductivity anomalies by way of aqueous fluids is tenable. These fluids may derive from the dehydration of serpentinite to peridotite in subducting oceanic crust,[7] amphibolite to granulite metamorphism in continental crust, the accretion of oceanic crustal rocks, or directly from the mantle (Glover and Vine 1995). The origin of high conductivity in stable continental crust, however, is enigmatic. Looking at a suite of representative locations, variations in the thermal and petrologic setting of these deep conductors has been pointed out by Wannamaker (2000), who suggests that a single thermally-activated mechanism is unlikely. Significant geophysical evidence suggests the presence of 1–3% aqueous fluids within the lower continental crust (Marquis and Hyndman 1992; Hyndman and Shearer 1989; Gough 1986; Hyndman and Hyndman 1968), with either saline brines and/or bicarbonate solutions posited to explain high bulk conductivities. These models, however, require permeabilities that are generally higher than thought reasonable for the lower crust, leading to difficulties in maintaining fluids over significant time scales (Hyndman and Shearer 1989; Nesbitt 1993). Following the cessation of metamorphism or tectonic activity, the residence time of deep-crustal water is on the order of 100 Ma, (Bailey 1990; Thompson and Connelly 1990). This finding, combined with the observation of enhanced lower-crustal conductivity in Precambrian shield terrances, has motivated modeling studies suggesting a geometry in which trapped fluids can be maintained over geologic timescales (Merzer and Klemperer 1992).

An additional argument against aqueous fluids in stable lower continental crust comes from petrology. Yardley and Valley (1997, 2000) argue that retrograde mineral reactions, occurring as rocks cool from their original equilibrium temperatures, will consume any traces of pore fluids remaining from peak metamorphic recrystallization. These arguments are not limited to a particular metamorphic facies and suggest a dry lower crust outside of active or recently-active tectonic regimes. While some of the identified deep conductors may reside in

[7] Conductivity anomalies within subduction zones and sutures are sometimes attributed to serpentinite, a product of low-temperature mafic metamorphism. Though waters released during dehydration may be conductive, the conductivity of serpentinite itself is moderate, rising to only 0.01 S/m at dehydration temperatures of 560°C (P = 600 MPa, Bruhn et al. 2004). Higher conductivities have been reported (Stesky and Brace 1973), but may be attributed to unusually high porosity or grain-boundary magnetite within the measured samples.

regions of brittle or semibrittle rheology (Wannamaker 2000) where fluids are more likely,[8] numerous examples of enhanced conductivity in stable, ductile lower-crust remain.

Graphite has been proposed as an alternate explanation for deep-crustal conductivity in stable terranes, and avoids the need to preserve fractures or pore space over geologic timescales. In the view of Wannamaker (2000), the onset of biogenic carbon deposition and plate tectonic collisional processes in the Proterozoic (Boerner et al. 1996) may have increased the input of carbon into the deep crust, which over hundreds of millions of years may have been episodically remobilized via seismic pumping (Sibson 1994) of hydrothermal C-O-H fluids to form long-range interconnected graphitic networks. This interpretation is not without debate, however, and concerns have been raised regarding the lack of graphitic films in exhumed lower-crustal rocks, the likelihood of sufficient and widespread carbonaceous fluids, and the tendency for such fluids to precipitate nonconductive carbonates rather than graphite (Yardley and Valley 2000). The origin of deep conductivity in stable continental crust continues to be debated among geophysicists, petrologists, and geochemists and remains one of the most important questions in earth sciences.

1.5 Advantages of an Integrated Interpretation

Determining lithology—the mineral composition and texture of rocks—is a common interest to a range of earth science disciplines. Geophysics, however, provides information not on lithology, but on physical properties. Distinct lithologies are commonly degenerate in one or more of their defining physical properties. This means that a many-to-one relationship exists between lithology and a given physical property. Thus, even with perfect data and a unique inverse solution (neither of which generally exist), lithology cannot be uniquely determined from a single geophysical technique. It is for this reason that geophysical methods are applied in combination, with the determination of multiple physical properties being used to break the degeneracy (Bosch 1999; Bosch et al. 2002). Granite and limestone, for example, have similar electrical conductivities, but differing magnetic susceptibility. In such a case, the additional information provided by magnetic surveying would permit discrimination between these two minerologies.

Limitations in the resolution of geophysical methods further the case for joint interpretation. Though magnetotelluric model assessment has been discussed, specific examples of spatial resolution are illustrative. Figure 1 shows the results of three synthetic inversion studies. In each case, the forward response of the model in the upper panel was calculated at a series of sites denoted by inverted triangles. The response data were contaminated with 2.5% Gaussian noise and then inverted using a smoothing-regularized inversion (Rodi and Mackie 2001). The optimal trade-off parameter (Eq. 8) was in each case determined from examination of an L-curve of data misfit versus model roughness, and the corresponding inverse model is displayed.

The first example illustrates the sensitivity of magnetotellurics to subsurface conductors. In Fig. 1a, a 1 km thick layer of 0.1 Ω m resistivity is embedded within a 100 Ω m halfspace. The synthetic inverse model in Fig. 1b accurately recovers the top of the conductor, however the bottom is poorly resolved. Magnetotellurics is most sensitive to integrated conductivity, or conductance. Thus, for example, a 1 km thick layer with 10 S/m

[8] Fluids at hydrostatic pressure have been encountered in several deep drill holes (Kremenetsky and Ovchinikov, 1986; Boresvsky et al. 1995; Emmerman and Lauterjung 1997) and fracture permeability is believed to increase markedly with measurement scale (Torgersen 1990).

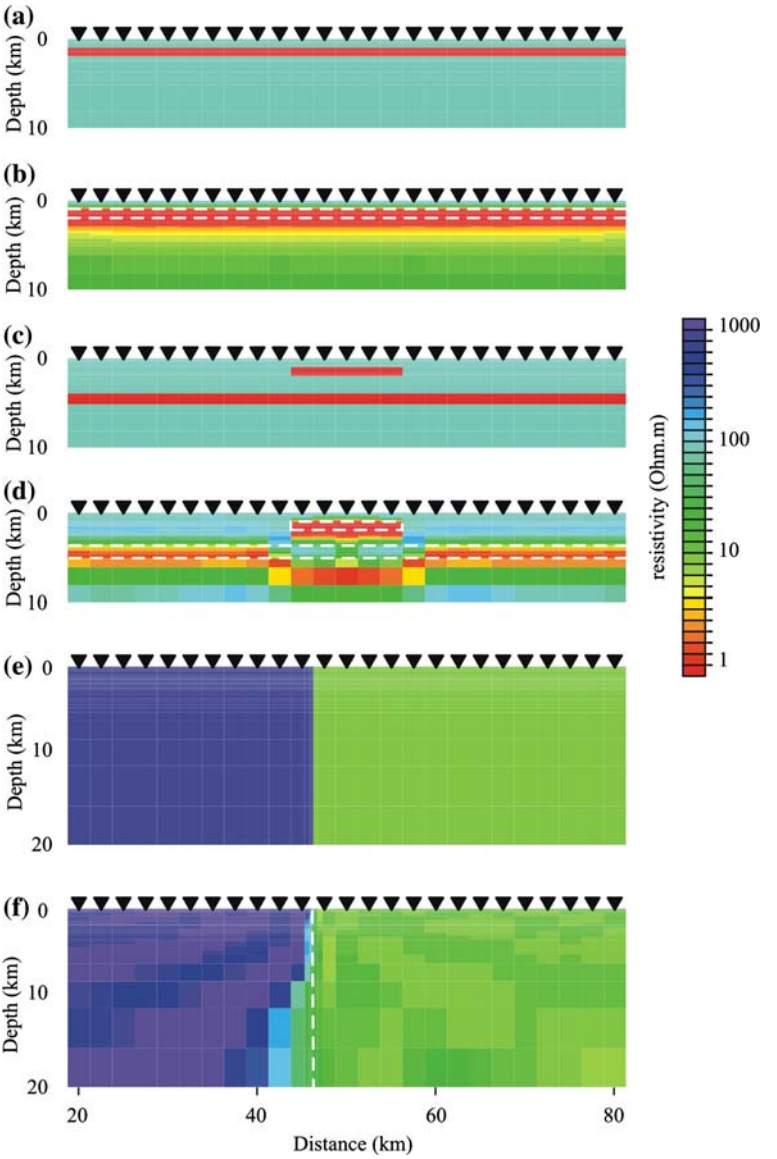

Fig. 1 Synthetic inversion study illustrating the limitations of magnetotelluric imaging. Resistivity models in **a**, **c**, and **e** were used to generate synthetic magnetotelluric data. These synthetic data were subsequently inverted using a minimum-structure inversion to produce the models shown in **b**, **d**, and **f**. Inverted triangles denote hypothetical station locations, while dashed lines outline boundaries from the original starting models. The sensitivity of magnetotellurics to conductance gives rise to a conductivity/thickness trade-off, in which the base of conductors is not well resolved (**a**,**b**). The screening effect of conductors can result in inaccurate recovery of deeper structures (**c**,**d**). Decreasing resolution with depth and smoothing regularization lead to diffuse boundaries (**e**,**f**)

conductivity has the same measured response as a 10 km thick sequence with a 1 S/m conductivity. In the example shown, the conductance of the synthetic inverse model is within 10% of that in the starting model. In a case like this, an independent constraint on

the base of the layer would uniquely constrain layer conductivity, thus permitting a more accurate assessment of both layer geometry and composition. The second example illustrates a screening effect, and was alluded to in an earlier discussion of model assessment. In Fig. 1c, a conductive layer is placed below an upper conductive block. In the synthetic inverse model in Fig. 1d, the underlying layer conductivity is underestimated near the edges of the conductive block and the layer is pushed to greater depth beneath the block. The final example presents a quarter-space model. In Fig. 1e, two blocks of dissimilar resistivity are joined along a vertical boundary. The synthetic inverse model in Fig. 1f recovers the vertical resistivity contrast well in the upper 5–10 km, but at greater depth the boundary appears to dip toward the left. This arises from a combination of decreasing resolution with increasing depth and the applied smoothing regularization.

Model sections and data pseudosections[9] are commonly displayed in color, permitting a rapid visualization of spatial variability. The human eye's perception of color, however, is non-uniform, and therefore determining additional information, such as what regions are considered anomalous, and where boundaries are likely to occur, can be quite subjective. The location of horizontal (vertical) resistivity boundaries are often best determined from curves of resistivity vs. depth (distance). The point of maximum gradient on the curve unambiguously defines a most probable location for a structural boundary. If coincident model sections of other physical properties are available, additional possibilities exist for more accurately defining structural boundaries. This is discussed in the section on quantitative interpretation.

The choice of color scale can also be misleading. Figure 2 shows a resistivity model on two different color scales; the narrow color scale (Fig. 2a) emphasizes subtle changes in model resistivity but has saturated the left-hand side of the model section, suggesting a simplified structure. In contrast, choosing a color scale that spans the full range of model conductivity (Fig. 2b) eliminates this saturation but results in visual suppression of subtle model features. It is therefore good practice to examine sections on several color scales in order to fully understand the variability within a model or pseudosection.

A final argument for a joint interpretation is to force a re-evaluation of the preconceptions we bring to all geologic or geophysical studies. There is an inclination toward models or findings that support our ideas, and in combination with a non-unique inverse problem and a plethora of regularization possibilities this can lead to 'cherry-picking' of the models that best confirm our ideas and hypotheses. The interpretion of data or models together with independent constraints, however, often requires a revision of our conclusions. Additionally, it may provide a richer understanding of limitations in processing, modeling and inversion. While an integrated interpretation may leave us with more questions than we started with, it provides a deeper understanding of the complexities and limitations of the data we are working with.

In what follows, case studies are presented which illustrate the added benefit afforded by an integrated, or joint, interpretation, as well as quantitative approaches to interpretation and inversion. Highlighted are innovative approaches to extract geologically meaningful information from physical property data and models. This review may thus serve as a guide to the integrated interpretation of magnetotelluric data. For the non-practitioner, this review highlights the power of the magnetotelluric technique and its capabilities in discerning earth structure, physical state, and processes.

[9] Pseudosections are plots of magnetotelluric response parameters, ρ_a and ϕ, versus frequency and distance along a profile. As frequency is a non-linear proxy for depth, pseudosections give a crude sense of how conductivity varies within the subsurface.

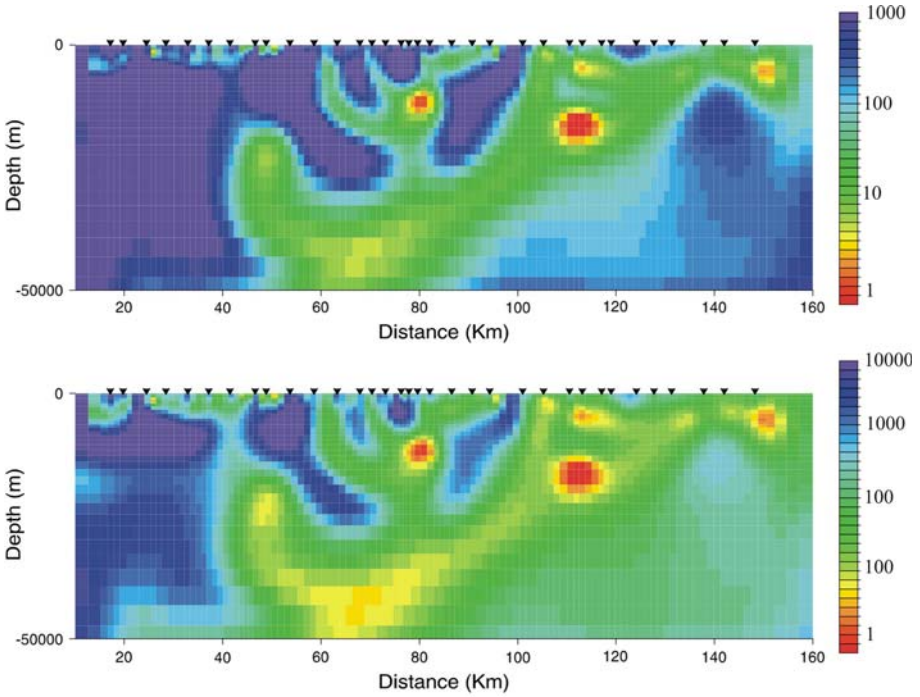

Fig. 2 Magnetotelluric resistivity model displayed on two differerent color scales. Upper panel has a narrow scale (1–1000 Ω m), resulting in saturation at the upper limit on the left side of the model. Lower panel has a wider scale (1–10,000 Ω m), causing subtle resistivity changes on the right side of the model to vanish

2 Case Studies

The breakdown chosen for assembling these studies is quite generic with studies crossing over into one another. Studies of structure and geometry are based largely on the conductivity *contrasts* within a model, and are commonly concerned with establishing or refining the location and geometry of lithologic and tectonic boundaries. Studies of physical, thermal, and compositional state are based on the inverted conductivity itself, and seek to place constraints on related variables such as porosity, salinity, melt fraction, viscosity, or temperature. Studies of earth processes are concerned with dynamics, and aim to better understand the range of earth processes including orogenesis, rifting, faulting, and subduction, whether in active or relic margins.

2.1 Studies of Structure and Geometry

Discerning earth structure is a primary goal of most geophysical studies. Structure in this sense refers to geometry and extent, whether it concerns faults, contacts, intrusions, sutures, or unconformities. An understanding of structure is a necessary prerequisite for testing process-related hypotheses and questions. For structural problems, an integrated approach amounts to blending independently-derived geometric constraints to arrive at a

structurally-conformal earth model or a consistent inference. This is typically a game of compare and contrast—a model or hypothesis supported by multiple data sets gains support, while one incompatible with one or more findings is deemed less plausible.

Seismic reflection sections provide structural constraints in terms of coherent impedance contrasts, which typically represent lithologic or hydrologic boundaries. They permit a visual interpretation of fault geometry, intrusion boundaries, salt diapirs, etc. What is often missing, however, is information on the material properties, i.e., what lies between the reflective boundaries.[10] It is in part for this reason that interpretations based on the combination of processed magnetotelluric and seismic reflection sections have been particularly successful. Reviews of early structural studies combining magnetotellurics and seismic reflection can be found in Jones (1998, 1987). This combination, for example, has significantly advanced our understanding of the continental lower crust (Hyndman and Shearer 1989; Jones 1992). For exploration purposes, magnetotellurics is combined with reflection studies for structural imaging in settings where seismic methods are hindered by strong scattering or low-velocity zones. These include carbonates or volcanic cover (Satpal et al. 2006; Withers et al. 1994), subsalt imaging (Key et al. 2006; Hoversten et al. 2000), and in overthrust belts (Orange 1989). As pointed out by Cook and Jones (1995), however, magnetotellurics and seismic reflection do not always provide information about the same horizons. They present an example in which borehole data defined a series of mafic sills emplaced within sulphide-rich argillite. Magnetotelluric data from the region were sensitive to variations in sulphide content while the resistive sills were not imaged. In contrast, seismic reflection sections revealed strong impedance contrasts from the tops of the sills but no reflections within the surrounding argillite. The differing sensitivity and averaging volumes of each method can give rise to such cases where enhanced conductivity and prominent reflections arise for very different reasons. Hence care must be taken when searching for structural conformity.

In the first of two examples from hydrocarbon exploration, gravity studies reveal an unexplored tectonic basin beneath the expansive Columbia River Basalts (CRB), which cover large portions of the northwestern United States. Interpretation of the gravity data was hampered, however, by lack of information on subsurface densities and little constraint on the thickness of the CRB. Equivalent gravity models were produced by both a thin CRB cover shallow basement and a thick CRB above a deeper basement. The irregular interbedded basalt flows also hindered seismic reflection profiling, resulting in discontinuous reflections that could not be reliably interpreted. Withers et al. (1994) showed that magnetotellurics, in contrast, was able to reliably estimate the base of the CRB as a transition from the resistive basalt to underlying conductive sediments. This boundary was imposed as a constraint in further gravity modeling, permitting a more unique structural model. Furthermore, the boundary was used as a marker horizon in re-interpreting the reflection data. These revised models were deemed favorable enough to drill a well which confirmed the thickness of the CRB to within 5% of the estimates determined from magnetotelluric models. The conductance of the underlying sedimentary unit was additionally found to be within 4% of that predicted.

Hydrocarbon exploration involving magnetotellurics is not limited to the determination of layer boundaries and sediment thicknesses. In an overthrust setting within the Rocky Mountain foothills, Xiao and Unsworth (2006) imaged an undulating conductive layer, the top of which follows folded Cretaceous sediments, as identified in seismic reflection

[10] While seismic velocities are determined during the migration of reflection data, they are not as robust as those obtained via refraction tomography.

sections. The conductivity was attributed to aqueous fluids based on well salinity measurements. Using the seismic reflection section as a guide, the authors noted that relative to the generally conductive sediments in the magnetotelluric section, higher conductivities were associated with anticlines and lower conductivities with synclines. They argue that this variation reflects increased (decreased) porosity and fracture permeability associated with extension (compression) along the hingelines of the anticlines (synclines), a finding observed in previous magnetotelluric surveys (Orange 1989). As permeability and porosity are important variables in reservoir characterization, the combined use of magnetotelluric and seismic reflection to map out their subsurface distribution is of great importance.

In the next examples, magnetotelluric-derived conductivity models are combined with seismicity in a range of tectonic settings. Aprea et al. (1998) imaged two prominent conductors associated with metasediments of the Olympic Core Rocks and the Seattle Basin in the Juan de Fuca subduction zone (Fig. 3). The sharp boundary between the Olympic Core Rocks (C1) and the Crescent Volcanics (R1) corresponds to both a steep gradient in Bouguer gravity (Finn 1990) and a prominent change in seismic velocity (Symons and Crosson 1997). These coincident changes in conductivity, density, velocity, and surface geology provide strong support for a deep-seated vertical fault or contact. The base of R3, believed to also be Crescent Volcanics, is undefined from the conductivity model alone, however seismicity outlines the subducting Juan de Fuca plate, and thus defines a lower limit to R3. Beneath the Seattle Basin, crustal seismicity is observed to fall exclusively within R3. Noting the absence of earthquakes in R1, the authors hypothesize that seismicity is not compositionally controlled. The spatial relationship between magnetotelluric model structure and earthquake hypocenters thus provides information on both structural configuration and earthquake generation.

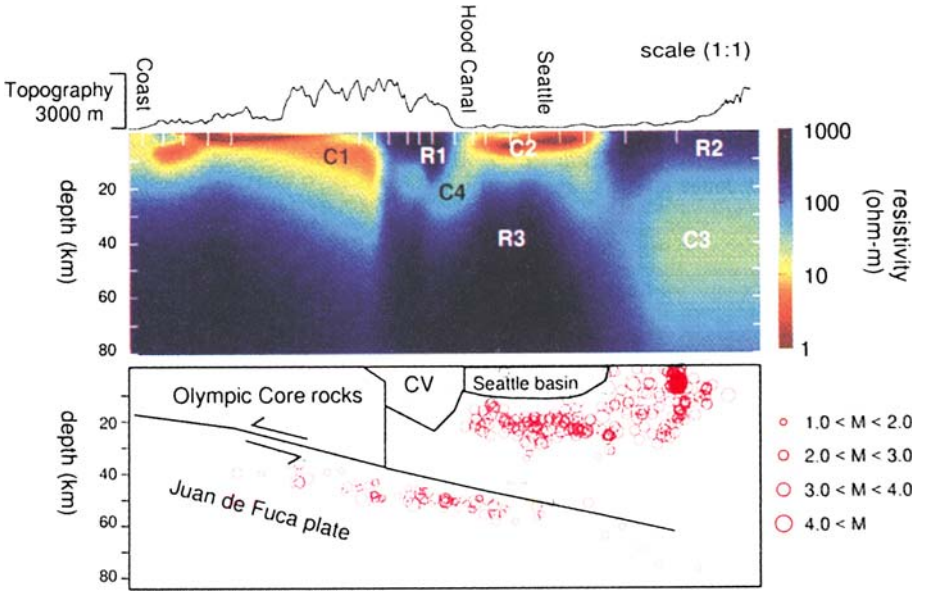

Fig. 3 Resistivity model from Aprea et al. (1998) and structural interpretation based upon it and earthquake hypocenters. Open circles in lower panel denote seismicity. CV = Crescent Volcanics. Olymic Core rocks are largely metamorphosed marine sediments originating in an accretionary prism. Conductors C1 and C2 reflect metasediments of the Olympic Core rocks and the Seattle Basin, respectively. Resistors R1 and R3 are attributed to the Crescent Volcanics

Along the India-Asia collision zone, Lemonnier et al. (1999) imaged a prominent conductor between 10 and 30 km depth beneath the Nepalese Himalaya (Fig. 4), noting that its position coincides with a crustal-scale fault ramp along the Main Himalayan Thrust. The location of this mid-crustal ramp was established through structural and geomorphic studies, and the presence of this ramp suggests that the conductor falls within a zone of intense deformation. More dramatic is the spatial coincidence between the top of the deep conductor and a cluster of seismic activity. Taken together, the authors argue that deformation along the mid-crustal ramp maintains a connected network for fluids released into the hanging wall of the fault. Dehydration reactions within the subducting Indian plate are believed to provide a continuous recharge of fluids which migrate upward into the brittle crust, giving rise to the observed microseismicity. It is the spatial relationship between the fault ramp, conductivity, and seismicity that permits the above interpretation and give insight into slab dehydration within this continent–continent collision zone.

Ogawa et al. (2001) similarly imaged a spatial separation between seismicity and several prominent conductors within a back arc setting in Japan. The imaged conductors are separated from each other by mapped thrust faults and correlate with seismic scatterers and low-velocity zones, leading the authors to conclude that the enhanced conductivity is due to aqueous fluids. The authors argue that the depth of fluids, together with the distribution of seismicity in proximity to the active thrust faults, suggests seismicity is related to migration of dehydration fluids into a less permeable crust. The mechanism suggested, in which thrusting progressively emplaces rocks below a depth where metamorphic dewatering reactions are accessible, was first proposed by Ague et al. (1998). Thus the identification of fluids from the magnetotelluric results provides an earthquake generation mechanism, while the earthquake distribution better delineates the boundaries of the imaged conductivity structure.

Using continuous magnetotelluric profiling, Unsworth et al. (1997) identified a flower structure within the upper 1–3 km of the San Andreas Fault in central California and attributed the enhanced conductivity within the fault zone to saline fluids. Using salinity estimates from a nearby well, the authors further estimated a range of subsurface porosities consistent with the imaged conductivity using Archie's Law (Eq. 10). It was the combination, however, of these results with tomographically-derived velocity models and regional seismicity that revealed a spatial separation between the high-conductivity, low-velocity fault zone and microseismicity. This recognition led Unsworth et al. (2000a) and

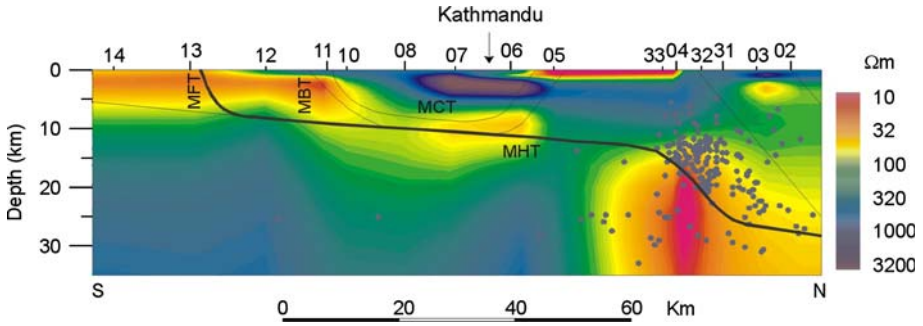

Fig. 4 Magnetotelluric resistivity model of the central Himalayas in Nepal from Lemonnier et al. (1999). Earthquake hypocenters (gray dots) from within 30 km along-strike are projected onto the section. Overlain geological section inferred from structural geology and geomorphic evidence of uplift. MFT = Main Frontal Thrust, MBT = Main Boundary Thrust, MCT = Main Central Thrust, and MHT = Main Himalayan Thrust

Bedrosian et al. (2002) to hypothesize that fluid-filled fractures, giving rise to the high conductivity and low velocities, also prevent the build up of shear stress necessary for brittle failure, thus limiting earthquakes to the boundaries of this region.

Within south-central Alaska, Fischer et al. (2004) imaged the aftershock zone of the 2002, M_w = 7.9 Denali Fault earthquake, which proved transparent to reflection studies. Despite the large magnitude earthquake, both aftershocks and regional seismicity terminate at shallow ($\sim$8 km) depth. Although this observation could be explained by high crustal temperatures leading to a shallow brittle-ductile transition, there is no supporting evidence for this scenario. The authors imaged a conductive volume that rises beneath the fault to within 10 km of the surface, close to the turn-off depth of seismicity. Alhough they do not speculate on a source, they argue that fluids attributed to the deep conductor may reduce rock friction, in a manner similar to that postulated at the San Andreas Fault, giving rise to the shallow seismicity cut-off. Together, this suggests that tectonic stress along the Denali Fault may be borne by an unusually thin brittle crust.

Along the subducting Cocos plate, a dipping conductor, the base of which could not be resolved, was imaged by Arzate et al. (1995) using magnetotellurics. In other subduction zones, such landward-dipping conductors have been found consistent with magnetotelluric data through forward modeling (Kurtz et al. 1986; Waff et al. 1988; Wannamaker et al. 1989), but the thickness of such a layer was poorly constrained (recall that magnetotellurics is insensitive to the base of strong conductors). Along the Cocos margin, low surface heat-flow constrains the temperature at the top of the conductor to 200–300°C, suggesting that dehydration fluids are not a likely cause. The authors examined the spatial relationship between the top of the conductor, earthquake hypocenters, a seismic low-velocity zone, and a modeled gravity interface, and found the dips of all these structures to be in rough agreement. A closer inspection revealed that the modeled gravity interface, corresponding to a density contrast of 0.7 g/cm^3 and interpreted as the top of the dense subducting plate is consistently 6–8 km beneath the top of the conductor. Together, this suggests the conductor is associated with a thick package of subducted wet sediment trapped between the overlying continental crust and the underlying oceanic plate. In this case, magnetotellurics and gravity data were needed to constrain the top and bottom, respectively, of the subducting sediments. Such information could be further used in a constrained magnetotelluric inversion to fix the conductor's base at the gravity interface. This could then be used to estimate sediment porosities, giving important estimates of the amount of water entering the mantle via subduction zones.

Where a sharp resistivity contrast exists between hanging- and foot-wall rocks, magnetotellurics can be combined with neotectonic studies to place bounds on fault offset, and in the presence of timing information, derive slip rate estimates. Bedrosian et al. (2001) examined crustal shortening and uplift within the Daxue Shan thrust range in northeastern Tibet. This range is one in a series of subparallel ranges accommodating slip along the eastern terminus of the Altyn Tagh Fault, a major strike-slip fault defining the northern boundary of the Tibetan Plateau. A magnetotelluric resistivity model (Fig. 5) imaged dipping conductors within the footwalls of two thrust faults, and the well-defined tops of these conductors constrain subsurface fault dips to within ±2°. Together with neotectonic studies (Meyer et al. 1998) and mapped surface geology, the fault geometry overlain in Fig. 5 was established. Interpreting the conductors as underthrust sediments, minimum bounds were placed on the amount of shortening along each fault. In combination with estimates of the onset of regional faulting (Metivier et al. 1998; Meyer et al. 1998), slip rates were estimated and then extrapolated to compare the combined slip rate accommodated across the thrust ranges to geologic and geodetic estimates of slip on the Altyn Tagh Fault.

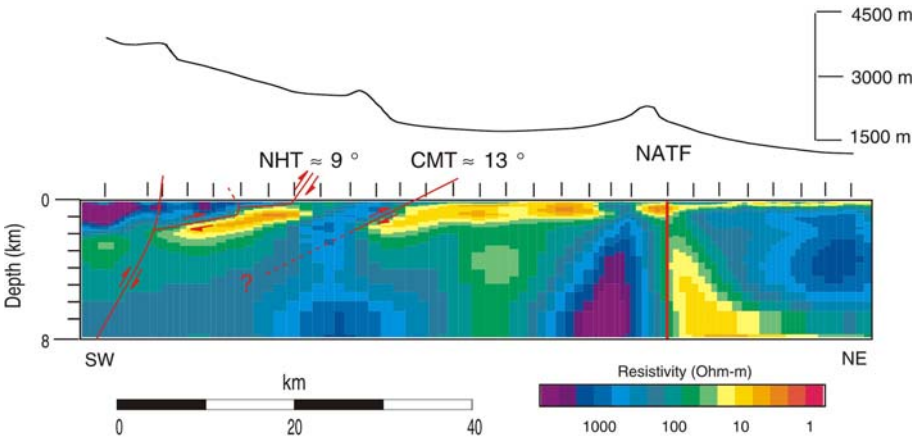

Fig. 5 Magnetotelluric resistivity model across the eastern terminus of the Altyn Tagh Fault, China. Southwest-dipping conductors are basin sediments emplaced within the foot walls of two thrust faults. Structural interpretation (in red) is based on surface geology, neotectonic studies, and the resistivity model. The fault-parallel extent of basin inversion provides constraints on the amount of thrust shortening. NHT = North Hills Thrust, CMT = Chang Ma Thrust, NATF = North Altyn Tagh Fault. Vertical exaggeration 2:1. Figure modified after Bedrosian et al. (2001)

In a similar fashion, Park et al. (2003) imaged conductive sediments of the Kochkor Basin (within the Kyrgyz Tien Shan), thrust beneath the crystalline range front along a gently dipping decollement. The extent of the underthrust sediments provided estimates of displacement along the decollement, while the geometry of the underthrust sediments helped to constrain a geologic cross-section that, in turn, was used to estimate total shortening across the basin margin. Dating of the underthrust sediments allowed the authors to further determine a long-term shortening rate which provides evidence that shortening in the region accelerated in the late Quaternary. It is the combination of magnetotellurics, structural geology, and age dating that are used to draw conclusions on fault kinematics.

2.2 Studies of Physical, Thermal, and Compositional State

These studies seek to determine measurable or derived physical properties; in the case of magnetotelluric measurements this commonly reduces to first determining the probable source of anomalous conductivity and then constraining secondary properties such as salinity, porosity, permeability, melt fraction, and viscosity. Independent information is included at both stages to reduce the ambiguity in the final interpretation. The thermal structure of the crust, a controlling factor in lithospheric dynamics, can be inferred from measurements of seismic attentuation or the analysis of xenolith data. Variations in seismic attenuation, though, are only a proxy for temperature, while xenoliths are unevenly distributed and their ascent history records a narrow window in space and time. More commonly, surface heat-flow measurements are extrapolated to depth assuming a particular geothermal gradient. This approach may fail, however, at active margins or where significant fluid migration (advection) is suspected (Mechie et al. 2004). As bulk electrical conductivity is strongly dependent upon temperature, magnetotellurics offers an independent means of estimating subsurface temperature.

Sutures, the remnants of plate collisions, have been found to be conductive over geologic time scales for reasons that are not fully understood (Tauber et al. 2003; Ritter et al. 2003b; Almeida et al. 2005; Boerner et al. 1996; Park et al. 1991). The late Jurassic-early Cretaceous Bangong-Nujiang Suture in Central Tibet is located within an active continent–continent collision zone, and hence its conductivity distribution may also reflect ongoing tectonic processes. As such, identifying the source of a mid-crustal conductivity anomaly (Solon 2000) requires careful thought. For a normal geothermal gradient, the temperature at the top of the conductor might be 600°C, making partial melt improbable, whereas an elevated geothermal gradient might allow this possibility. What is needed to constrain composition is an independent estimate of subsurface temperature. In quartz-rich rock, the α/β quartz transition depends on pressure and temperature, and is largely independent of other mineral assemblages in the rock. It is furthermore accompanied by significant changes in the elastic properties of quartz, which allowed Mechie et al. (2004) to identify it via wide-angle seismic reflection. As shown in Fig. 6, the α/β quartz transition at ~18 km depth is only a few km above the region of high conductivity. At the seismically determined depth, this transition correponds to 700–800°C, implying a minimum geothermal gradient of 39°C/km. Therefore the top of the imaged conductor is at 800–900°C, well within the range of wet felsic melt.

South of the Bangong-Nujiang Suture, a significantly deeper α/β quartz transition (~32 km) implies lower-crustal temperatures consistent with aqueous fluids or partial melt. Li et al. (2003) exploited constraints from a wide range of geologic and geophysical data to explain the widespread high conductivity imaged within the lower crust beneath

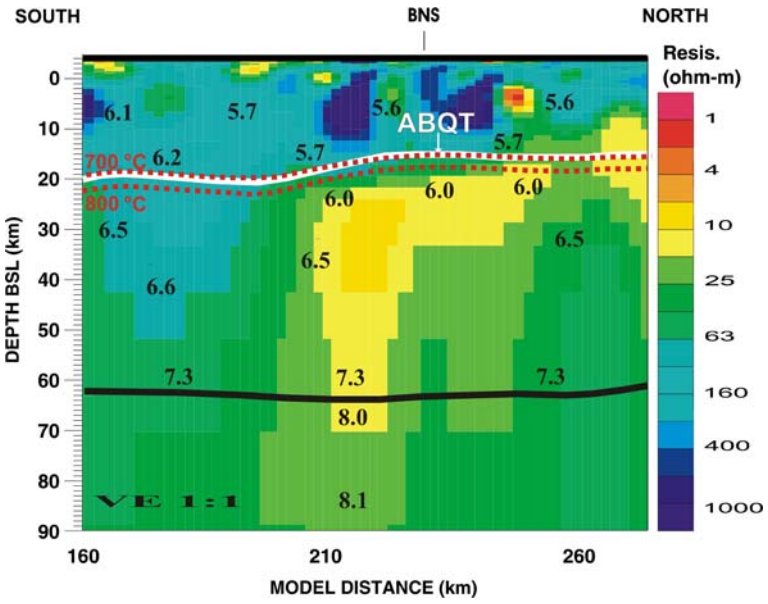

Fig. 6 Magnetotelluric resistivity model of the central Tibetan Plateau overlain with independent seismic results. ABQT denotes the location of the α/β quartz transition defined by seismic reflection data. P-wave velocities (in km/s) and the crust/mantle boundary (black line) from the seismic model of Zhao et al. (2001) are also indicated. Note the correspondence between the ABQT and the top of the mid-crustal conductor, explained by a few percent wet felsic melt. BNS = Bangong-Nujiang Suture. Figure reproduced from Mechie et al. (2004) using a resistivity model modified after Solon (2000)

Southern Tibet (Wei et al. 2001; Unsworth et al. 2005). Using a series of constrained inversions, the minimum conductance required by the magnetotelluric data (6000 S) was established. One hypothesis is that the conductance is caused solely by aqueous fluids. Choosing an upper limit for fluid conductivity (100 S/m) and the most-connected fluid distribution, the authors calculate bulk conductivity as a function of porosity. Reflection coefficients from seismic bright spots near the top of the conductor (Makovsky and Klemperer 1999) are consistent with aqueous fluids and porosities of $\sim$15%. Together with the conductance constraint, these porosities result in a minimum layer thickness of $\sim$1 km. Another hypothesis is that the conductance is caused solely by partial melt. Again choosing an upper limit for melt conductivity (10 S/m) and a well-connected melt distribution, the authors calculate bulk conductivity as a function of melt fraction. Seismic refraction data image a $\sim$20 km thick low-velocity zone at mid-crustal depths that may be due to partial melt (Kind et al. 1996). Using the thickness of this zone and the minimum conductance estimate, a 20 km thick layer of partial melt requires $\sim$4% melt.

In both of the above end-member scenarios, explaining the minimum conductance involves a trade-off between fluid fraction and layer thickness that could not be resolved without the addition of independent geophysical constraints. In the case of aqueous fluids, porosity was constrained, leading to an estimate of layer thickness, whereas in the case of partial melt, the layer thickness was constrained, resulting in an estimate of melt fraction. To evaluate these hypotheses, the authors noted petrologic findings that question whether significant amounts (>0.1%) of aqueous fluids can be maintained at mid-crustal depths (Yardley 1986; Yardley and Valley 1997, 2000). Support for partial melt comes from the velocity tomography, a satellite magnetic low indicative of a shallow Curie depth (Alsdorf and Nelson 1999), high surface heat flow (Francheteau et al. 1984), and geodynamic modeling that finds partial melt to be a consequence of crustal thickening (Beaumont et al. 2001). The authors finally conclude that the anomalous conductance is most likely due to a thick layer of partial melt (>10 km) locally overlain by a thin layer (100–200 m) of aqueous fluids.

Widespread conductivity anomalies are generally due to aqueous fluids and/or partial melt, however, as discussed in the introduction, localized anomalies may also be attributed to conductive mineralogies. Using magnetotellurics, Wannamaker and Doerner (2002) imaged an undulating conductor within the Basin and Range province in northeastern Nevada. This conductor is exposed west of the profile and is identified with a highly folded and faulted shale sequence (Fig. 7). The high conductivity may be due to graphite, a metamorphic product of carbon-bearing shale requiring elevated pressures and temperatures. Although this region is not interpreted to have undergone appreciable burial and metamorphism, shear deformation has been found to catalyze graphitization at significantly lower pressure/temperature conditions (Nover et al. 2005; Ross and Bustin 1990). This is consistent with the inverse model shown in the left panel of Fig. 7, in which conductivity is highest in the folded western region. The shale thickness is well constrained from surface geology and borehole measurements, leading the authors to fix this variable in subsequent forward modeling to determine along-profile variations in shale conductivity and layer geometry. The resulting model is shown in the right panel of Fig. 7. In both the inverse and forward models, an eastward decrease in shale conductivity is evident. Together with an eastward increase in total organic content (i.e., a decrease in graphite), this trend is taken to reflect a varying degree of hydrocarbon maturation along the profile, a result with implications for regional hydrocarbon exploration.

Up to this point, we have concentrated on examples in which the source(s) of anomalous (high) conductivity must be identified. By looking at a region of resistive lower crust and

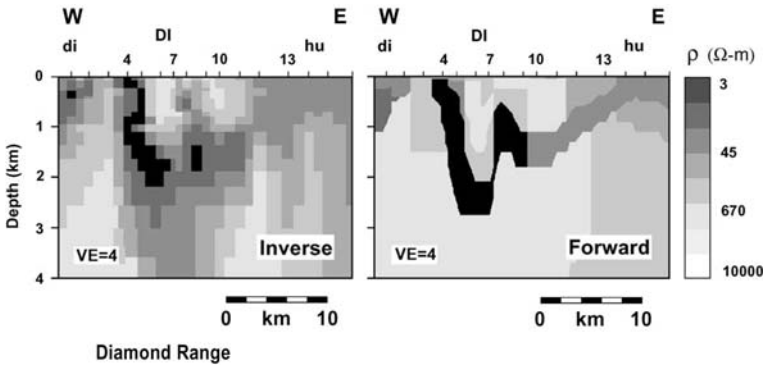

Fig. 7 Magnetotelluric inverse (left) and forward (right) resistivity models of northeastern Nevada from Wannamaker and Doerner (2002). Near-surface low resistivities are attributed to graphitized shales. DI = Diamond Mountains., di = Diamond Valley, hu = Huntington Valley

upper mantle, Ledo and Jones (2005) combined laboratory conductivity measurements and mineral composition to bound upper-mantle temperature within the Canadian Cordillera. In magnetotelluric surveys, a resistive crust precludes the possibility of screening effects (as discussed in the introduction) and a resistive upper mantle assures an accurate estimate of conductivity. At the depths investigated and in the absence of partial melt or aqueous fluids, bulk rock conductivity is due to solid-state conduction. It is dependent to first order on temperature, mineral composition, and the geometric distribution of the individual minerals. For a pyrolytic composition (Irifune and Ringwood 1987), the major conductive minerals in the upper mantle are olivine, orthopyroxene, and clinopyroxene. For a fixed temperature and mineral distribution, the relationship between composition and bulk conductivity can be expressed by a ternary diagram. Conductivity of the pure mineral phases as a function of temperature was determined by a solid-state Arrhenius Equation based on laboratory measurements (Xu and Shankland 1999; Xu et al. 1998). Since the geometric distribution of minerals is unknown, the authors applied the Hashin–Shtrikman bounds (Eq. 9) for a three phase system at three temperatures (800, 1000, 1200°C). As shown in Fig. 8, the upper and lower bounds are quite close, reflecting the fact that the conductivity difference between the three pure mineral phases varies only by a factor of six. We now have relationships between composition, temperature, and bulk conductivity. Using mantle xenoliths from the region (Abraham et al. 2001), the authors determined an average composition, allowing them to bound the upper mantle temperature to 820–1020°C within this region.

Combining magnetotellurics with laboratory conductivity measurements in a completely different way, Evans et al. (2005) examined mantle composition in a marine environment near the East Pacific Rise. An anisotropic inversion strategy (Baba et al. 2006) produced models showing the conductivity structure parallel to the spreading ridge as well as in the spreading direction. These models (not reproduced here) cover a section of oceanic lithosphere spanning 1.3 to 4.5 million years in age. They show (a) an increase in oceanic mantle conductivity at 60 km and (b) anisotropic conductivity below this depth with enhanced conductivity in the spreading (flow parallel) direction. Since the 60 km boundary is independent of plate age (i.e., it is consistent along the entire profile), the resistivity change is not likely to be thermal in origin.[11] To explain the nature of this

[11] A thermal explanation would imply that the boundary deepens with increasing plate age as the plate cools.

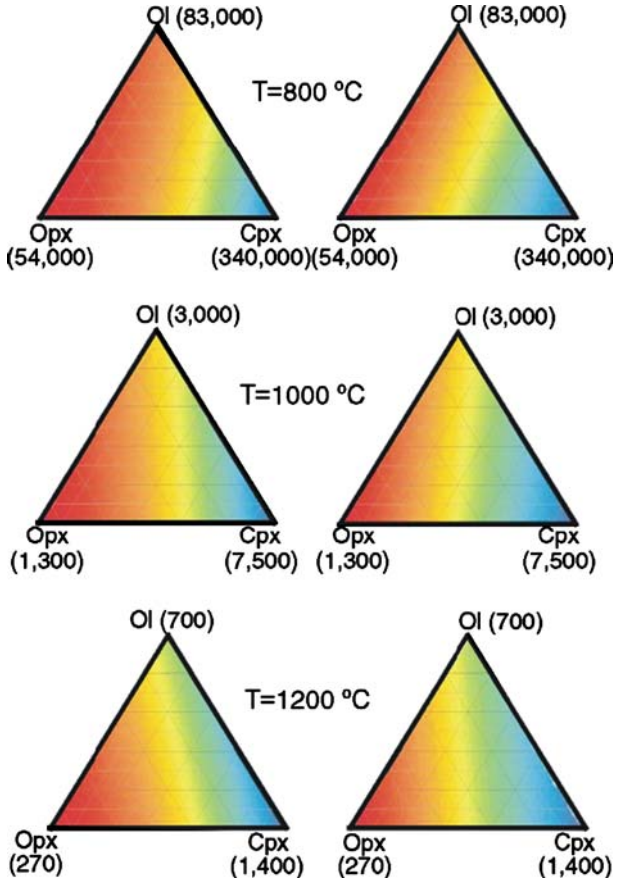

Fig. 8 Ternery diagrams of resistivity using the Hashin–Shtrikman lower (left) and upper (right) bounds for Ol–Cpx–Opx mantle rocks. Values in parentheses are the electrical resistivity in Ω m of each mineral at the given temperature. The color scale at each temperature is relative and ranges from more conductive (red) to more resistive (blue). Figure from Ledo and Jones (2005)

boundary as well as the electrical anisotropy, the authors began by comparing laterally-average conductivity-depth profiles (from the inversion model) to laboratory-based profiles for dry peridotite at an assumed mantle temperature of 1350°C. As shown in Fig. 9a, dry peridotite is too resistive to explain the magnetotelluric findings. The authors then proposed that hydrogen diffusion in olivine, a major mineral constituent of peridotite, might explain both the observed conductivity increase and its anisotropy at depth. The anisotropic conductivity of olivine, due to anisotropic hydrogen diffusivity, was first described by Karato (1990). For example, the [100] axis of olivine containing 1000 ppm hydrogen has the necessary (higher) conductivity. Figure 9b shows conductivities predicted by the Nernst–Einstein equation for hydrogen diffusion along all three crystallographic axes of olivine; the [100] axis is parallel to the spreading direction based upon lab measurements and shear-wave seismic splitting experiments. Altogether the increased mantle conductivity and anisotropy beginning at 60 km reflects a change from dehydrated to hydrated peridotite with 50% alignment of olivine. In this example, the original magnetotelluric

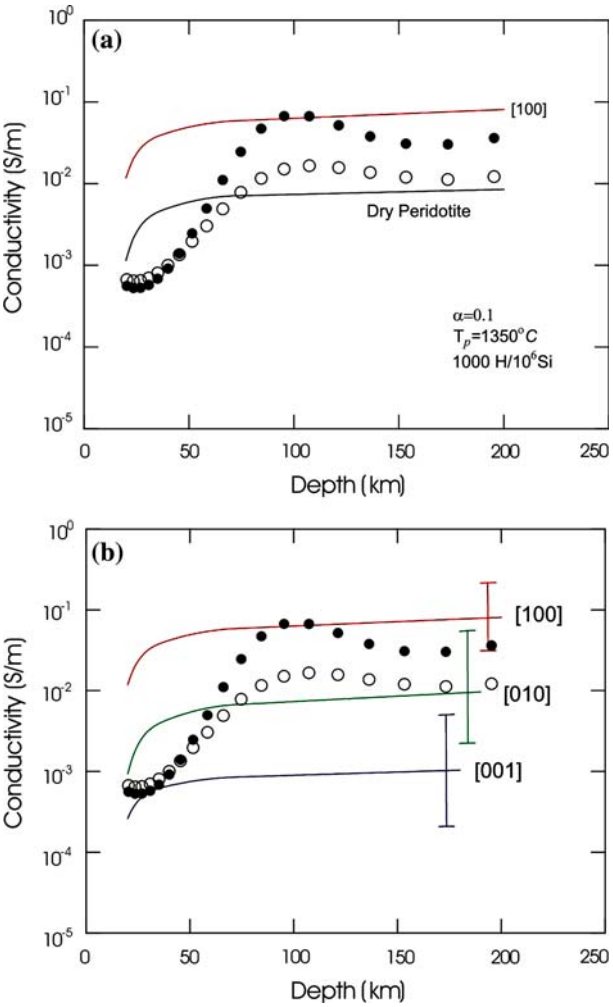

Fig. 9 Laterally-averaged conductivity-depth profiles in comparison to laboratory-based conductivity measurements on peridotite. Black and white circles denote anisotropic ocean bottom conductivity in the spreading direction, and parallel to the ridge, respectively. (**a**) Conductivities predicted for dry peridotite (black line) and for wet peridotite (red line) using the Nernst–Einstein equation for hydrogen diffusion along the [100] axis of olivine. (**b**) Conductivities along all three crystallographic axes of olivine. Wet peridotite conductivity calculations assume 1H/10^{3}Si. The [100] axis is parallel to the spreading direction as determined from seismic splitting experiments. Figure modified from Evans et al. (2005)

model shows an intriguing conductivity and anisotropy transition which provides the necessary information to elucidate mantle compositon at depth.

2.3 Studies of Earth Processes

The sensitivity of bulk conductivity to aqueous fluids and melt allows magnetotellurics to go beyond structure and physical state to provide insight into earth processes. Subsurface

fluids play an important role in a host of processes; by imaging their distribution, magnetotellurics can inform a range of processes including faulting and mineralization (Heinson et al. 2006; Tuncer et al. 2006; Hoffmann-Rothe et al. 2004; Wannamaker et al. 2002), magmatism and metamorphism (Wannamaker and Doerner 2002; Park and Mackie 2000), slab dehydration (Wannamaker et al. 1989; Kurtz et al. 1986; Booker et al. 2004; Brasse et al. 2002), and salt-water intrusion (Falgàs et al. 2006; Unsworth et al. 2000b).

In a marine environment, the dynamics of melt generation have been examined through magnetotelluric studies of seafloor spreading across the East Pacific Rise (Key et al. 2002; Evans et al. 1999). Key et al. (2002) imaged a crustal conductor beneath the spreading ridge axis, spatially coincident with both a zone of low P-wave velocity determined from seismic tomography (Dunn et al. 2000) and a region of low S-wave velocity determined from seafloor compliance measurements (Crawford and Webb 2002). Applying mixing laws to the bulk conductivity of this zone (1–10 Ω m) and assuming a well-connected melt geometry gives estimates of 1–20% partial melt. Using the seismic results to define the boundaries of the melt zone, the authors conclude that melt is confined to a region from 1.5 to 6 km depth within 3 km of the ridge axis, resulting in an estimate of 0.75 km^3 of crustal melt per kilometer of ridge. Estimates such as these can be used in combination with plate spreading rates to determine melt residence times, which provide important controls for thermal and geodynamic models of crust formation.

The creation of new oceanic crust is extremely localized when compared to the far-reaching deformation associated with convergent plate margins. Continent–continent collision zones produce some of the most spectacular topography on earth, yet due to the heterogeneity and long accumulated history of continental crust, they remain one of the least understood aspects of plate tectonics. In examining the collision of the Indian and Asian plates, several hypotheses for plateau formation and evolution may explain how the lithosphere deforms: whole-scale subduction (Argand 1924; Willett and Beaumont 1994), distributed crustal thickening (Dewey and Burke 1973), lithospheric delamination (Molnar 1988; England and Houseman 1989), and lower-crustal flow through vertical decoupling of the crust (Clark and Royden 2000). Each of these hypotheses has implications for subsurface structure. Nelson et al. (1996) combined a wealth of geophysical data to produce a detailed view of convergent processes in the Himalayan region. In Fig. 10, the geometry within the model section is constrained by seismic reflections and the shear wave velocity profiles help constrain the crust to mantle transition (Moho). An expansive mid to lower-crustal conductor imaged via magnetotellurics was identified with a partially molten middle crust by Li et al. (2003) as discussed in a previous section. In addition to crustal thickening, the partial melt suggests a weak middle crust decoupled from both the mantle lithosphere and the overlying upper crust. Such a vertical decoupling allows the middle crust to flow laterally in response to plate convergence, giving rise to east–west extension. These conclusions, though derived from a range of techniques, were based on a single north–south profile, making extrapolations about regional structure questionable.

For the middle crust to flow, geodynamic models require both strain localization and a viscosity decrease of nearly an order of magnitude (Beaumont et al. 2001). To determine whether such a decrease is plausible, Unsworth et al. (2005) combined bulk resistivity structure determined via magnetotellurics with laboratory strain measurements to estimate the viscosity of a partially-molten middle crust. Three additional profiles in the northwest Himalaya and southern Tibet spanning 1500 km along strike confirmed that partially-molten middle crust is ubiquitous. In Fig. 11a, the measured resistivity of the partial melt in each region is indicated by dashed lines. Using the results of Li et al. (2003), the resistivity of pure melt was fixed to the range 0.1–0.3 Ω m. Using an approach analogous to Schilling

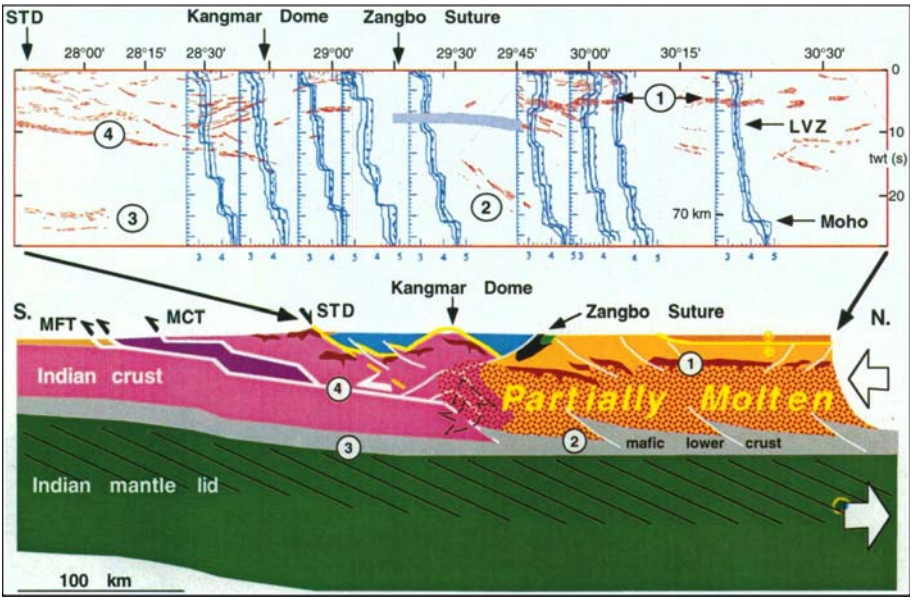

Fig. 10 Composite geophysical image from Nelson et al. (1996) of evidence for convergent geologic processes in southern Tibet. Blue lines in upper panel are one-dimensional shear wave velocity profiles overlain upon composite reflection section in red. Blue bar indicates wide-angle reflections north of the Zangbo Suture. Numbers refer to (1) mid-crustal partial melt layer as identified from reflections, low shear-wave velocities, and magnetotellurics, (2) possible Moho imbrications based on steeply dipping deep-crustal reflections, (3) reflection Moho, and (4) the Main Himalayan Thrust. LVZ, low velocity zone; MFT, Main Frontal thrust; MCT, Main Central thrust; STD, South Tibetan detachment system

et al. (1997), solid curves denoting bulk resistivity as a function of melt fraction were constructed. Their intersections indicate that less than 5% melt is required to explain the modeled conductivity beneath the northwest Himalaya but 5–14% melt is required for southern Tibet. In Fig. 11b, laboratory measurements on granite and aplite provide estimates on the scale of viscosity changes accompanying increases in melt fraction. For the southern Tibet profiles, a viscosity decrease of nearly an order of magnitude is expected for the upper limit (14%) of calculated melt fractions, consistent with the requirements of geodynamic models. It is unclear, however, how laboratory measurements at strain rates of 10^{-5} s^{-1} correspond to strain rates of 10^{-15} s^{-1} associated with convergence in the Himalayan region. Nonetheless, these studies are an example of how magnetotellurics can be integrated with geophysical and geologic data to address questions of crustal-scale deformation.

The Altiplano-Puna Plateau, formed by the collision of the Nazca and South American plates, is similar to the Tibetan Plateau in altitude, areal extent, and underlying crustal thickness. Over both geologic (Allmendinger and Gubbels 1996) and geodetic (Klotz 2000) time scales, the upper crust between the Western and the Eastern Cordilleras appears to move as a stable block. To determine if subsurface rheology controls this movement, Brasse et al. (2002) began with magnetotelluric imaging. In Fig. 12, an expansive conductor beneath the Altiplano is clearly seen in the model. Its top surface varies between 10 and 30 km depth and correlates well with seismic reflection data. Its lateral extent is roughly bounded by the Western and Eastern Cordilleras. As stated by the authors, "The

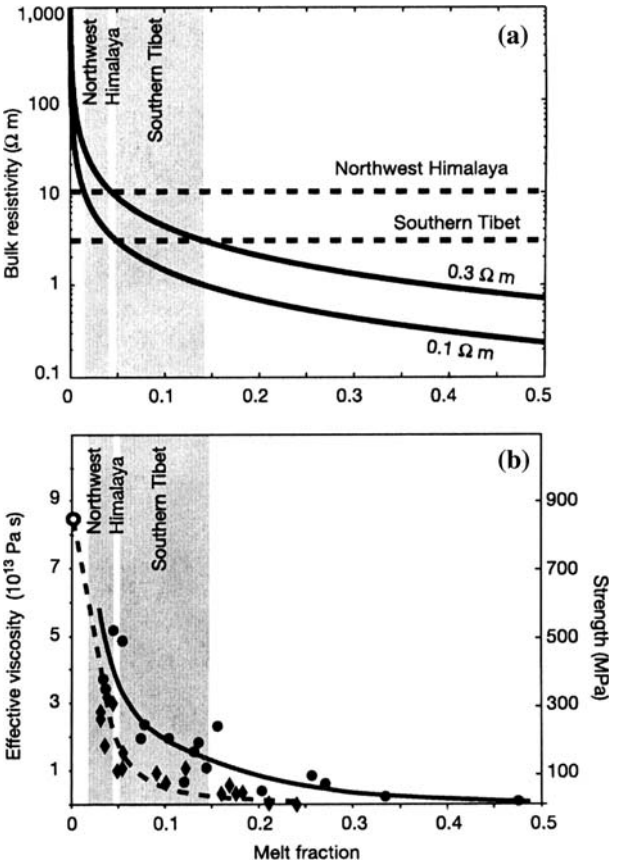

Fig. 11 Magnetotelluric constraints on the mechanical strength of partially molten rock as related to the Tibetan lower crust. (**a**) Bulk resistivity as a function of partial melt (solid lines) for pure melt resistivities of 0.1 and 0.3 Ω m. Dashed lines indicate average bulk conductivity from magnetotelluric inverse models; shaded regions denote the range of permissible melt fractions corresponding to these bulk conductivities. (**b**) Effective viscosity and rock strength as a function of melt fraction based on lab measurements of granite (*circles*) and aplite (*diamonds*). Figure reproduced from Unsworth et al. (2005)

key to understanding the impressive conductivity anomaly below the Altiplano derives from the comparison with the results from other geophysical methods." Noting high heat flow densities (>100 mW/m^2, Hamza and Muñoz 1996; Henry and Pollack 1988), low seismic velocities (10–20% reduction, Yuan et al. 2000), strong seismic attenuation (Q_P < 100, Haberland and Rietbrook 2001) and elevated V_P/V_S ratios ($\sim$1.8, Rietbrock and ANCORP Research Group 1999), the authors conclude that a 10–14% wet granitic melt best satifies the diverse geophysical measurements. Such a high melt fraction implies decreased viscosity within the middle and deep crust, similar to the findings of Unsworth et al. (2005) described above. As such, the magnetotelluric results combine with other geophysical data to suggest that the upper crust rafts upon a rheologically weak layer.

The generation and transport of metamorphic fluids associated with active crustal thickening is examined by Wannamaker et al. (2002) in the context of the New Zealand Southern Alps, a young compressional orogen parallel to the Alpine Fault (Walcott 1998).

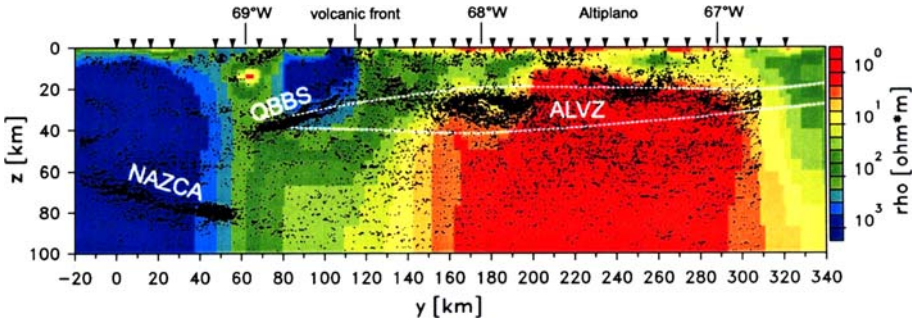

Fig. 12 Magnetotelluric resistivity model of the central Andean margin from Brasse et al. (2002). The top of the Altiplano conductor coincides with seismic bright spots (black lines) and a low-velocity zone (ALVZ). The descending Nazca slab (NAZCA) and the Quebrada Blanca bright spot (QBBS) reflections are uncorrelated with the resistivity model

Geologic evidence suggests that significant uplift has occurred within 25 km of the Alpine Fault, with the highest grade Alpine Schists exposed from depths of 19–25 km (Grapes 1995). Hydrothermal veining and gold deposition associated with a deep-crustal fluid component are furthermore localized parallel to the Alpine Fault. A range of geophysical studies including, gravity and passive seismology have identified a deep-crustal root extending to 40 km depth beneath the orogen. Magnetotelluric modeling and inversion complete the picture, imaging an orogen-scale zone of high conductivity at mid- to lower-crustal depths, the deepest parts of which overlap with this crustal root. This broad conductive zone shallows beneath the Alpine Fault, rising subvertically to within 10 km of the surface, near the base of the seismogenic zone. The enhanced conductivity, too high to be explained by solid-state conduction in dry silicate rocks, is attributed to an interconnected grain-boundary phase, likely aqueous fluids and/or graphite. The combination of these diverse findings paints a picture of metamorphic fluid genesis and syn-tectonic flow. The advection of cooler material to depth within the crustal root leads to prograde metamorphism and the release of fluids. These fluids are likely held at lithostatic pressures beneath the brittle-ductile transition, except near the Alpine Fault, where the uplifting schists permit the episodic release of fluids into the overlying brittle crust. The mixing of these reducing fluids with oxidized meteoric waters results in gold precipitation within vein deposits. This coherent story is only possible through the intersection of geophysical, geological, and geochemical evidence.

A final example by Booker et al. (2004) provides constraints on subduction-zone processes along a flat-slab segment of the subducting Andean margin. The authors imaged, as shown in Fig. 13, a vertical conductor rising from the mantle transistion zone (410–660 km) to within 100 km of the surface at the easternmost edge of the flat-slab region. Forward modeling, in which a thin resistor was inserted at 300 km depth (horizontal dashed lines) thus cutting the conductive path from the deep mantle, resulted in a significant rise in data misfit. As discussed in the introduction, this represents a necessary yet insufficient condition for eliminating the possibility of such a resistive break. Extrapolating shallow seismicity to deeper Benioff-zone hypocenters, the authors noted the correspondence between the inferred slab position and the conductor. Combining plate convergence rates with the timing of volcanic cessation, the authors concluded that the subducted slab from the surface to 400 km depth has never been below active volcanism and thus may retain significant volatiles. The vertical conductor may therefore reflect the release of fluids at

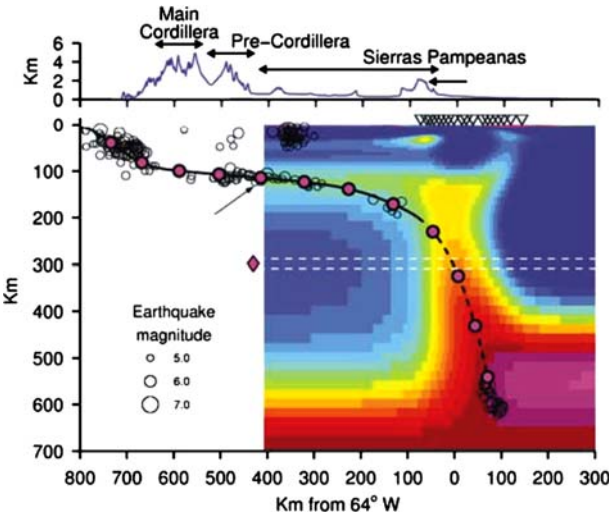

Fig. 13 Magnetotelluric resistivity model beneath central Argentina from Booker et al. (2004). Magnetotelluric stations are denoted by *inverted triangles*. Earthquake hypocenters (*open circles*) define location of the subducting slab, dashed where inferred. Filled circles denote 1 Ma isochrons along the slab since the time of subduction

250 km depth and nearly 1000 km from the trench, inducing partial melting within the overlying South American lithosphere. An alternative interpretation was stimulated by the observation of a conductivity contrast across the slab within the mantle transition zone. The authors suggest this is evidence of a 'water-filter' model, in which there is pervasive upwelling of mantle fluids through the transition zone, while the upper mantle remains (relatively) dry (Bercovici and Karato 2003). The model predicts a dry (resistive) upper mantle, such as that being dragged down with the Nazca slab, and a hydrated (conductive) transition zone, as seen beneath the South American Plate. This transition zone may only require a small amount of volatile input from the descending slab in order to initiate partial melting, evidenced by the imaged vertical conductor.

3 Quantitative Methods of Integrated Interpretation and Inversion

3.1 Statistical Methods

The methods described herein serve as a bridge between many of the qualitative comparisons previously discussed and the constrained multi-property inversions discussed in the following section. Similar to the above studies, they are based on a combined interpretation of post-inversion models. The assumptions, limitations, and errors in the processing are thus folded in with the model or result. A gravity model, for example, may have an excellent fit to the data, but a constraint taken from it, such as the depth to basement, is dependent upon the data reduction, the knowledge of subsurface rock densities, and a priori structural information. Statistical methods take a quantitative approach, with the end goal being a more accurate determination of lithology through the examination of multiple physical properties.

Scatter plots of electrical resistivity and seismic attenuation values taken from coincident models were examined by Haberland et al. (2003). They found several regions where these properties were highly correlated and used them to identify distinct regions of partial melting (low resistivity, high attenuation) beneath the Altiplano plateau. A similar approach was applied to coincident resistivity and seismic velocity sections by Maercklin (2004) and Bedrosian et al. (2004), who used regions of high correlation to define hydrologic and tectonic boundaries.

A classification approach (Schalkoff 1992) similar to that used in medical imaging, can be applied to coincident, geophysical models (Bauer et al. 2003). The methodology as developed by Bedrosian et al. (2007) is sketched in Fig. 14. Coincident and independently-derived geophysical models are first interpolated onto a common grid. An inverse model can be thought of as an ensemble of point values, each associated with a particular location. Interpolation thus results in a set of co-located model points, each identified with two or more physical properties and a unique subsurface location. Together with error estimates in the model parameters at each point, a probability density function (pdf) is assembled in the joint parameter space (JPS). Classes are subsequently identified as localized regions of enhanced probability density and then mapped back to the spatial domain (a depth section) where each class is interpreted as a distinct geologic structure (lithology).

This method was applied to upper-crustal magnetotelluric and seismic models of the Dead Sea Transform (Ritter et al. 2003a). Bedrosian et al. (2007) used these independently-derived models, together with error estimates in model resistivities and velocities from the sensitivity matrix, and ray density, respectively. As shown in Fig. 15a, the assembled pdf shows localized regions in the JPS of high probability density. Classification was achieved

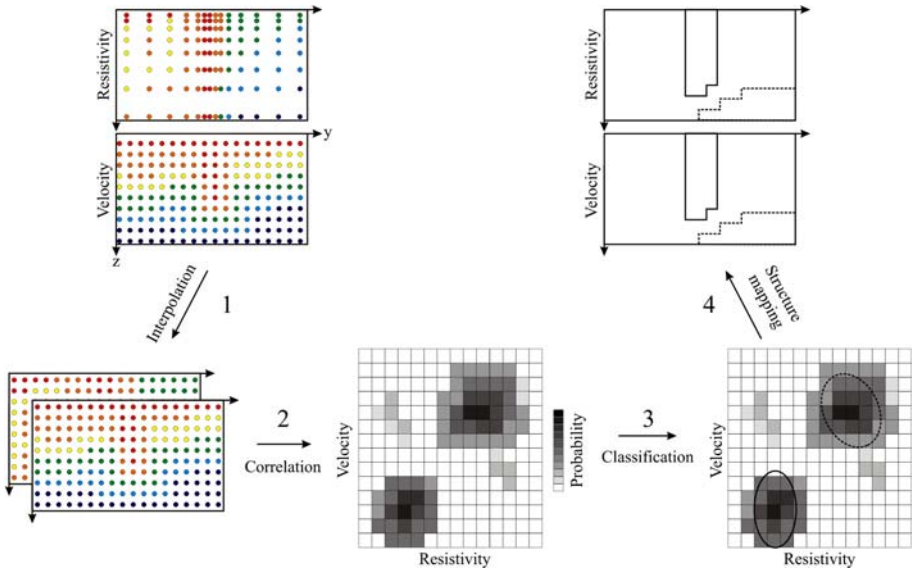

Fig. 14 Probabilistic approach to structure classification using independent geophysical models. Independent models are interpolated (1) onto a common grid. The correlation between the models is examined (2) and significant classes (localized regions of high correlation) are identified (3). Classes are then mapped back onto the depth section (4) and interpreted as distinct lithologies. Figure modified from Bedrosian et al. (2007)

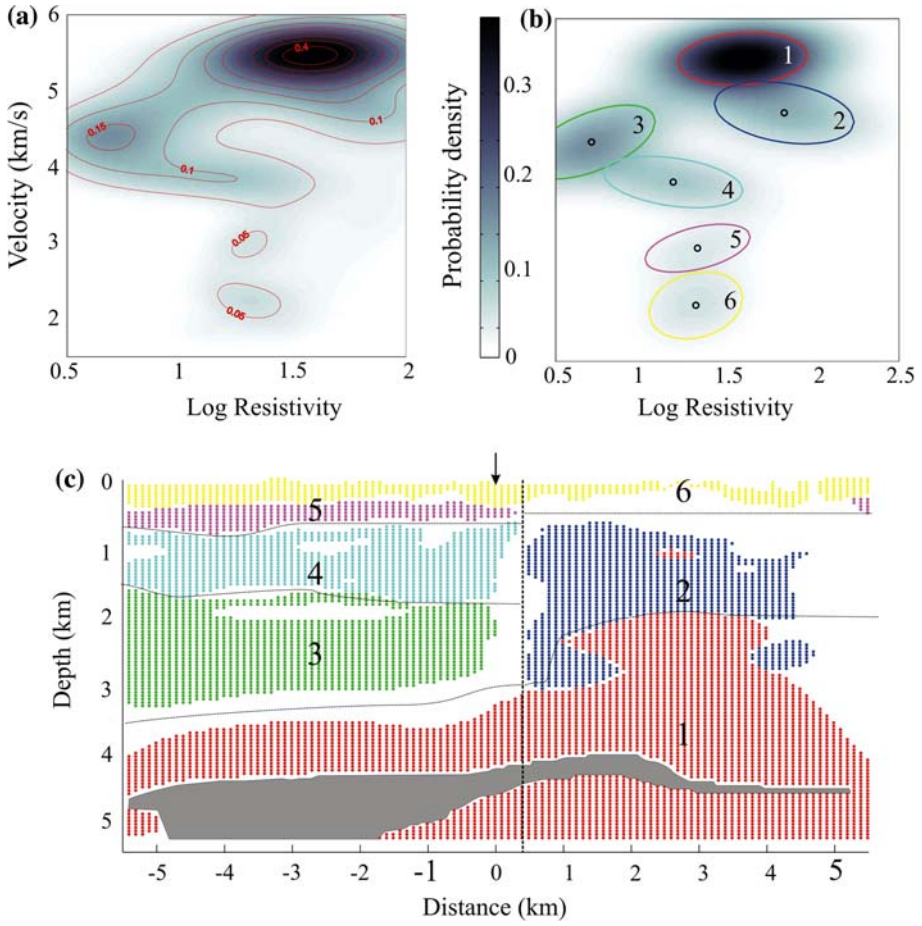

Fig. 15 Structure classification applied to coincident magnetotelluric and seismic refraction models. (**a**) pdf assembled from the interpolated model points and their respective errors, with contours indicating probability density. (**b**) nonlinear parametric fit to the pdf in (**a**) together with 1σ class boundaries. (**c**) depth section identifying structures by color as defined in (**b**). Grey region indicates missing model data, where the method could not be applied. Figure from Bedrosian et al. (2007)

by fitting the calculated pdf to a sum of bivariate Gaussian functions and defining class boundaries by their 1 sigma errors (colored ovals in Fig. 15b). Upon mapping these classes back onto the model section, distinct structures were outlined as horizontal, spatially well-connected regions. Four of the six classes further correspond to structures cut vertically by the Dead Sea Transform. In combination with surface geology and well log data, each structure was identified with a distinct lithology. The advantages of this approach are threefold. First, class identification does not rely upon subjectively-defined boundaries from color model sections. Second, each resulting class is characterized by a range in the joint parameter space, facilitating lithologic identification of the class using, for example, petrologic data (Bauer et al. 2003). Third, realistic error estimates, reflecting the spatially non-uniform resolution of the model parameters, and by extension, of the individual methods, are included in the analysis.

Independent of this work, Tronicke et al. (2004) developed a similar statistical classification technique to integrate post-inversion physical property models. Their technique differs from the previous in two important respects. First, the authors employ K-mean cluster analysis (MacQueen 1967) to classify the joint parameter space. This approach partitions the JPS into a predefined number of non-overlapping classes, and does not assume a specific statistical distribution. Second, the approach of Tronicke et al. (2004) does not permit the inclusion of errors in the model parameters—thus the effects of spatially-variable model resolution cannot be accounted for. An extension of this work by Paasche et al. (2006) makes use of fuzzy cluster analysis (e.g., Höppner et al. 1999), permitting points in the JPS to have partial membership in multiple classes. This approach is more flexible in defining class membership, as all model cells are not automatically forced into a class. Classes with split membership are thus analogous to regions outside of the Gaussian confidence intervals in the approach of Bedrosian et al. (2007).

3.2 Constrained Multi-property Inversion

Inversion remains the workhorse of geophysical data interpretation. The previous section concerned the correlation of distinct and independent *models*, that is, post-inversion. Much recent work focuses on integrating independent geophysical information during the inversion process to produce models consistent with all the data and imposed constraints. It is informative to consider inversion from the perspective of reducing the space of potential physical property models in search of the true earth model. Figure 16 depicts a region of model space consistent with observed data to within a given tolerance. A point in model space is taken to represent a unique combination of one or more physical properties defined at a series of subsurface locations. The extent of the acceptable model space reflects the non-uniqueness of the inverse problem, and is a function of data coverage, data errors, modeling assumptions, and method resolution. The true earth model is assumed to fall within this region. Regularization, imposed to stabilize the non-unique inverse problem serves to narrow the permissible model space, selecting out a subspace of models consistent with our choice of regularization (e.g., minimum-curvature models). When multiple data sets or external information (borehole logs, surface geology, etc.) are available, these may be used to further reduce the acceptable model space, either through imposing additional regularization, or by steering the inversion in

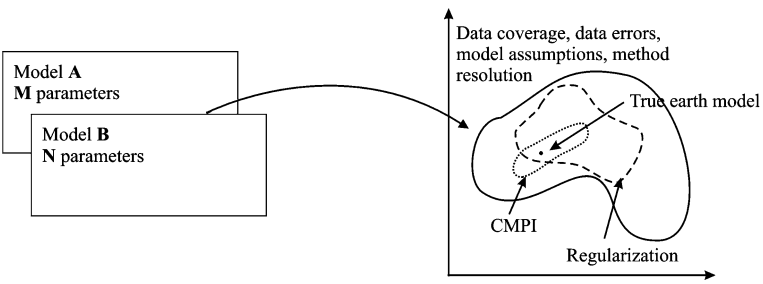

Fig. 16 Acceptable model space for geophysical inversion. Physical property models A and B, consisting of M and N model parameters, respectively, can be represented as a point within an M + N dimensional model space. The solid line depicts the region of model space consistent with the data to within a given tolerance. Imposing regularization narrows the acceptable model space (*dashed line*). Linkage between the models or their underlying data sets further narrows the model space (*dotted line*)

a more ad hoc fashion. By shrinking the model space, the linkage of independent data sets provides a means with which to minimize the resolution deficiencies of individual methods while maximizing their strengths. As such, a properly formulated constrained multi-property inversion reduces model non-uniqueness and improves parameter estimation.

From a mathematical persepective, joint inversion involves solving for multiple physical properties at a set of model cells based on multiple data sets. It is an expansion of the objective function (Eq. 6) to include the misfits of both data sets, and does not implicitly specify any interaction between the independent data sets or resulting models. Without a coupling between the data or models, there is no added benefit to such an inversion over single-property inversions. For this reason I will avoid the term joint inversion, and instead refer to what follows as constrained multi-property inversion (CMPI), where a coupling is explicitly required. CMPI is thus an inversion where multiple physical properties are determined using regularization or constraints to couple the data, physical properties, or model structure.[12] Constrained inversion, used to test features during model assessment, can be thought of as an end member of CMPI. Though only inverting for a single physical property, by modifying and fixing part of a model in accordance with independent information, we are manually 'steering' the inversion by asking for the model that best fits the data subject to the imposed constraint. The fundamental question of CMPI is how to establish links between the independent data, physical properties, or model structure.

We proceed by looking at the case of combining magnetotellurics and seismic refraction methods, as both provide images of earth structure at comparable scale and resolution. A data linkage (between travel times and MT transfer functions) is not straightforward and has not been considered to date. Several authors have, however, attempted to link electrical conductivity and seismic velocity on theoretical or empirical grounds. Schmeling (1986) derived mathematical linkages between electrical and elastic properties, however, the work is limited in scope to regions of partial melting. CMPI can likewise be formulated around an assumed petrophysical relationship, however such relationships cannot often be determined, at best hold locally, and are dependent upon an array of secondary unconstrained variables. The use of effective medium theory to develop a parameterization of velocity and resistivity applicable to upper-crustal regions shows some promise. These parameterizations are based upon porosity, pore aspect ratio, and interconnectivity, as well as properties of the host rock and pore fluid. Such relations may be able to provide a fuzzy mapping between resistivity and velocity (i.e., a particular resistivity may be compatible with a range of seismic velocities dependent on porosity, aspect ratio, etc.).

The variation of physical properties due to weathering, fracturing, and the chemical alteration of earth materials are complex, and better accounted for by empirical relations. Examination of crossplots of conductivity and velocity from well-log data have in some cases shown striking correlation in the joint parameter space. Dell'Aversana (2001) was able to fit a global relation to such data, which was used to convert a velocity inverse model into a resistivity model subsequently used as a starting model for magnetotelluric inversion. The success of this study, however, was due in part to the relatively homogeneous structure sampled by the well logs. Such model conversions between two physical properties are more common in the inversion of seismic refraction and gravity data (Parsons et al. 2003; Roecker et al. 2004), where empirical relationships between velocity and density are of more general applicability (Gardner et al. 1974; Christensen and Mooney 1995).

[12] This is sometimes referred to as cooperative inversion (Lines et al. 1988).

The correlation of independent magnetotelluric and seismic refraction models, as illustrated in the previous section, show no simple empirical relation, but rather a series of localized correlations in the JPS, each interpreted to represent a distinct lithology. Such information can be used as the basis for a zonal inversion, in which a sparsely parameterized physical property model, consisting of a limited number of distinct lithologies or zones, is sought (Hyndman et al. 1994). Paasche and Tronicke (2007) have applied this approach to CMPI, taking advantage of class-membership criteria derived from fuzzy clustering analysis to update model parameters. For each data set, an iteration of a grid-discretized, single-property inversion is followed by reduction to a zonal model via cluster analysis. The discretized physical property model is updated according to Eq. 11, where the jth parameter within the kth physical property model (p_{kj}) is replaced with a membership-weighted (m_{ij}) average of the (c) class means (μ_{ki}).

$$p_{kj} = \sum_{i=1}^{c} m_{ij} \times \mu_{ki} \tag{11}$$

The optimal number of classes are determined by examining an L-curve of data misfit versus number of classes. In this method the results of structure classification can be drawn upon in the inversion process, though they are not embedded (as a regularization) within the inversion itself.

Model linkages provide one of the least restrictive means with which to link a constrained multi-property inversion while still honoring the individual data sets. In the absence of known or derived relationships between the physical properties, the spatial coincidence of boundaries or transistion zones may still be used to link the models (Lines et al. 1988). Monteiro Santos et al. (2006) used simulated annealing, a global optimization technique, to invert resistivity and gravity data for layered-earth structure, assuming common layer boundaries. Their method treats the resistivity data as one-dimensional and requires a priori specification of the number of layers and their densities, thus leaving the interface locations and layer resistivities as unknown parameters. Synthetic tests show it better resolves layer interfaces than the separate inversion of each data set, thus reducing some non-uniqueness in the solution. A similar approach has been used by Manglik and Verma (1998) for the 1D inversion of magnetotelluric, seismic refraction, and seismic reflection data. These 1D approaches can be viewed as a type of adaptive mesh inversion, in which the inversion parameters include the model mesh itself (layer thicknesses). The extension of this technique to two and three dimensions is unclear, though adaptive mesh techniques are under development for the 2D magnetotelluric inverse problem (Key et al. 2006).

A different structural approach to CMPI, more applicable to 2D and 3D inversion, was examined by Haber and Oldenburg (1997). Their regularized inversion scheme seeks to minimize a model structure penalty function (ϕ_m) of the form

$$\phi_m = \sum_{i=1}^{M} \left(S[m_1^i] - S[m_2^i] \right)^2, \tag{12}$$

where m_1^i and m_2^i represent the ith cell of the two physical property models being inverted. This penalty function is summed over the M model cells and measures the difference in structure *between* the models, where the normalized structure operator, $S[m]$, based upon model curvature, is given by

$$S[m] = \begin{Bmatrix} 0 & |\nabla^2 m| < \tau_1 \\ P_5(|\nabla^2 m|) & \tau_1 < |\nabla^2 m| < \tau_2 \\ 0 & |\nabla^2 m| < \tau_2 \end{Bmatrix}. \tag{13}$$

P_5 is a degree five polynomial with coefficients chosen to ensure that $S[m]$ is continuous and twice differentiable. These conditions are necessary for the iterative, linearized inversion algorithm the authors employ. As defined, the structure operator is always positive and normalized on the interval [0,1]. This ensures that positive and negative model curvature are treated equally, and that ϕ_m is insensitive to an overall scaling of the models. Thus, for example, a peak in one physical property model coincident with a trough in another model are considered structurally conformal, and are not penalized. A limitation of this method is that τ_1 and τ_2, which define the target model roughness interval, must be chosen carefully. If τ_1 is too large, the model structure penalty function will remain ineffective until considerable model roughness has been attained. Conversely, if τ_1 is too small, and τ_2 is too large, the entire model space will be regarded as having structure, and the penalty function will guide the inversion toward concordant models at all roughness scales.

A more serious limitation of this and any of the previous approaches is the underlying assumption that changes in one physical property model are accompanied by changes in another. As illustrated in the previous section, multiple lithologies may be degenerate in one physical property while separable in another (horizontal or vertical lines in Fig. 15a). Additionally, as pointed out in an earlier example (Cook and Jones 1995) different methods may be sensitive to different mineralogic or hydrologic phases, hence structural conformity is not always to be expected, and should be enforced if and only if all data sets can be adequately fit by a conformal model. Consider, for example, a two-layer earth model where layers 1 and 2 differ in physical property A but have identical values of physical property B. Inverted separately, data set A produces physical property model A, with a required boundary between the two layers. Data set B forbids such a boundary and inversion will result in a homogeneous model of physical property B. A CMPI based upon the structure penalty function in Eq. 12, however, will steer the inversion toward structurally concordant physical property models, either producing homogeneous models (with a higher misfit to data set A), or those with a layer boundary (and a higher misfit to data set B).

A less restrictive approach which relaxes the requirement of coincident changes in model structure is that of Gallardo and Meju (2007). Their approach is similar to that of Haber and Oldenberg (1997) in that they present a structure-linked CMPI, however their inversion uses a cross-gradient model-structure operator (ϕ_m) to measure the structural similarity between the models:

$$\phi_m = \sum_{i=1}^{N} \nabla m_1^i \times \nabla m_2^i. \tag{14}$$

The null values of this cross-gradient structure operator define *either* full colinearity or the absence of gradients within one or both models. It is this last null condition that permits accurate recovery of models in situations such as the two-layer case described above. The homogeneous physical property B has zero gradient, hence (ϕ_m) is minimized and the required gradient in physical property A remains unaffected. It is only when both data sets require non-vanishing gradients that the stucture penalty function steps in to enforce colinearity of the gradients. A consequence, however, of using an unnormalized operator is

that the colinearity of larger gradients will be more actively enforced than smaller gradients during the inversion.

Figure 17 illustrates a synthetic model the authors use to demonstrate the enhanced resolving power of the cross-gradient approach. The model includes structural details that are difficult to resolve via the individual techniques. For magnetotellurics, it is the thin resistive channel between conductors C and D, that due to screening effects, is difficult to resolve. For seismic refraction, it is the boundary between low velocity (B) and high velocity (C, E, F). The diffraction of rays around low-velocity body D results in an absence of rays to adequately image this boundary.

Figure 18 shows the resistivity and velocity models derived from separate and linked inversions. In the resistivity model (Fig. 18a), the conductors C and D are smeared together, while in the velocity model (Fig. 18b), the upper boundary of the basement, C, is poorly resolved. In the models derived from the linked inversion, the thin resistive channel is recovered (Fig. 18c) and the low to high velocity transition (Fig. 18d) is much sharper. Enforcing structural conformity via the cross gradient operator improved other subtle features in each inverse model, more accurately reflecting the synthetic starting model in Fig. 17. This is apparent from the structural similarity between the resistivity and velocity models, as measured by the cross-gradient operator (Eq. 14), the value of which is displayed for the independently inverted models (Fig. 18e) and the linked-inversion models (Fig. 18f). With this type of linkage the deficiencies in spatial resolution associated with each method can be partially overcome.

An alternative approach to model-structure linked CMPI is to search for models that have similar spatial continuity (but are not necessarily structurally conformal) as measured by a geostatistical model. Such a geostatistical (variogram) model may be based on ground-truth, well logs, or an independent geophysical model, and can be used to regularize an inversion. This formulation, termed stochastic regularization, imposes stochastic properties on undetermined portions of an inverse model (Maurer et al. 1998) through the covariance matrix ($2C_m$, Eq. 8). The traditional smoothing ($\bigtriangledown^2 m$) and damping (similarity to a prior model) regularizations can be viewed as end-members of stochastic regularization assuming strongly correlated and uncorrelated model parameters, respectively. Outside of these end-member cases, the calculation of $2C_m$ for an arbitrary geostatistical model is computationally intensive. However, given uniform grid discretization and a stationary variogram, methods exist for the efficient calculation of $2C_m$ (Dietrich and Newsam 1997). Linde et al. (2006) applied stochastic

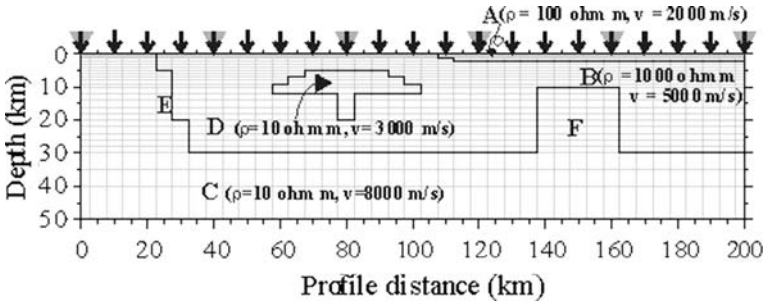

Fig. 17 Synthetic starting model and grid design for the cross-gradient inversion of Gallardo and Meju (2007). Model resistivities and P-wave velocities are given for model features A–F. Magnetotelluric stations denoted by arrows; seismic shot points denoted by inverted triangles

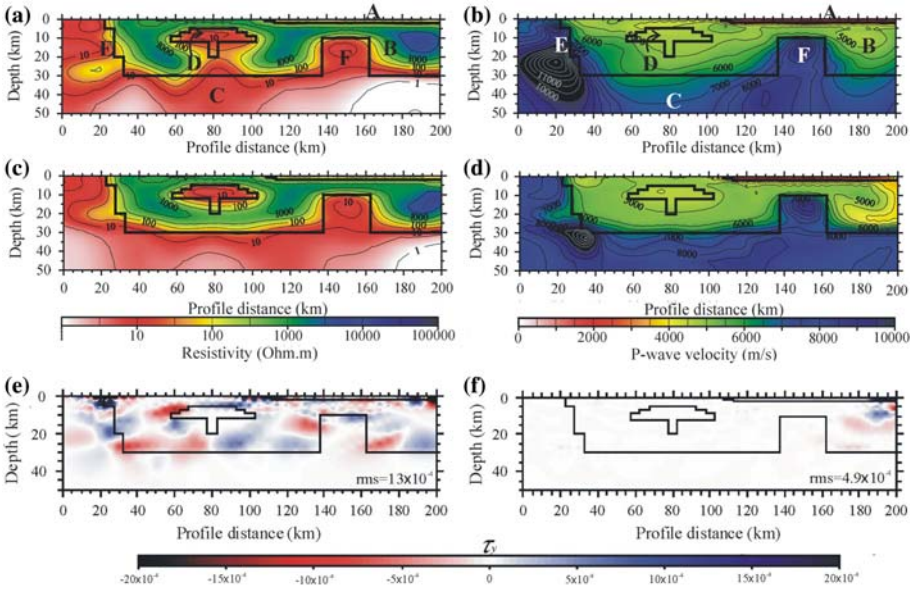

Fig. 18 Magnetotelluric and seismic velocity models recovered by separate inversions (**a**,**b**) and by a cross-gradient linked CMPI (**c**,**d**). Thick black lines outline structures within the starting model (Fig. 17). Panels (**e**) and (**f**) show structural similarity, as measured by the cross-gradient function (Eq. 14), between the magnetotelluric and seismic models obtained via separate and linked inversions, respectively. Note the increase in structural conformity provided by the CMPI. Figure modified after Gallardo and Meju (2007)

regularization to the inversion of cross-hole electrical resistance and ground-penetrating radar data, using conductivity logs and zero-offset traveltime data to define geostatistical models. The authors included separate covariance matrices for each physical property model and additionally imposed a cross-gradient constraint (Eq. 14) to link the models during their inversion. In principle, however, stochastic regularization derived from a single geostatistical model could itself provide the model-structure linkage for a CMPI.

4 Discussion

An integrated interpretation combines independent information to draw more informed conclusions regarding earth structure, physical state, and processes. The types of information combined, their errors and limitations, and the desired output all play a role in the approach to integration.

4.1 Sources of Information

The information we combine depends on the problem at hand. Structural studies require spatial information, as we are primarily interested in geometry. Geophysical inputs include

magnetotellurics, seismic reflection, refraction, and earthquake seismology, as these all produce subsurface images. When incorporated as processed models, they have the assumptions and limitations of the techniques, processing, and inversion wrapped into them. Geologic information includes surface mapping, balanced cross sections, and well logs. Such information is characterized by uneven sampling (surface-based) or undersampling (limited well coverage).

When physical, thermal, or compositional state is the goal, constraints on material properties are of primary interest. Physical properties derived from magnetotellurics, seismic refraction, seismic attentuation, and magnetic surveying are supported by laboratory measurements of conductivity, velocity, attentuation, and susceptibility on samples of known composition at relevent subsurface conditions. It is typically the combination of field and laboratory measurements through petrophysical relationships that permit determination of physical state and composition (mineralogy, porosity, melt fraction, etc.). Magnetotellurics, seismic attentuation, surface heat-flow data, geochemical closure temperatures, and xenoliths all provide information on the thermal structure of the subsurface, important to understanding earth dynamics.

Understanding earth processes requires a rich knowledge of both structure and composition. These studies typically draw upon all available information to develop models capable of discriminating between competing hypotheses. Geodynamic modeling plays an important role in these studies, as computer simulations are capable of testing the effect of variations in physical and thermal state on the evolution of tectonic processes that in the earth occur over geologic time scales. Analog modeling is likewise important in understanding the complex deformation of real materials in a controlled setting that can then be compared to geophysical and geological observations.

4.2 Types of Integration

The integration of data can be thought of in terms of how information is used during combination. As this review concerns the integrated interpretation of magnetotelluric data, one source of information is always assumed to be derived from magnetotellurics. As such, a discussion of integration boils down to how independent information is treated during the modeling and inversion of magnetotelluric data. More generally, this breakdown applies to any non-unique modeling or inverse study in which we seek to narrow the region of acceptable model space (Fig. 16) based on multiple sources of independent information.

In what follows it is important to remember that all infomation brought to bear on a problem have associated errors. Measured data have statistical and systematic errors, be it a seismic waveform, a measured fault dip, or a chemical concentration. The reduction and analysis of data can introduce further uncertainty in the results due to limitations in the data set (limited sample size, narrow frequency band, undersampling, etc.) or approximations and assumptions in the analysis. When concerned with modeling and inverse problems, assumptions regarding earth complexity (subsurface dimensionality), model parametrization, trade-off parameters, and the choice of regularization further compounds data errors.

4.2.1 Qualitative, Post-analysis

Many of the studies discussed in this review fall within this category. In this case, additional information does not affect the analysis itself, only interpretation of the results. For example, several studies were presented in which the interpretation was predicated upon an

observed spatial separation between crustal conductors and earthquake hypocenters. These studies assume both that the boundaries of the conductors are well constrained and that the hypocenter locations are accurate. There may, for example, exist a conductivity model that fits the magnetotelluric data equally well but places a conductor directly over the earthquake hypocenters. Alternatively, the hypocenters may have absolute location errors large enough to invalidate any spatial correlation. An advantage of a post-analysis approach is that it derives from independent results—thus consistent structure is in no way contrived or selected during the analysis. A disadvantage is that errors in the individual results and the non-uniqueness of the inverse problem are not taken into account during integration.

4.2.2 Hard a priori Constraints

The incorporation of information into modeling/inversion as a hard constraint involves fixing model parameters or their gradients within the starting model, thus requiring that the constraint be incorporated into any inverted models or responses. In the example by Wannamaker and Doerner (2002), the thickness of the shale sequence, based upon surface and borehole measurements, was used as a constraint in a series of forward models (Fig. 7). The constraint was then used to narrow the subspace of potential conductivity models by searching for a model consistent with the independently determined layer thickness. Another example is seen in the study by Brasse et al. (2002), where the location of a prominent seismic reflector associated with the subducting Naza slab is observed without a corresponding resistivity signature (Fig. 12). To test whether a conductor parallel to the reflector is consistent with the magnetotelluric data, the authors added this feature to the model (not shown), and used this modified model as the prior model in the objective function of Eq. 8. A damping-regularized inversion thus attempts to find a model that fits the data and is most similar to the prior model. The authors found the conductor was removed in the resulting inverse model, and therefore its presence is inconsistent with the data. This approach is attractive in that a subspace of alternate models are examined in response to the added constraint. It is, however, restrictive in how we chose to represent the constraint in the starting or prior model. In the last example, for instance, a 10 km thick conductor was considered. It remains unknown if a model with a thinner conductor or a simple discontinuity in conductivity may still fit the data.

4.2.3 Soft a priori Constraints

Soft a priori constraints are less restrictive in that they do not explicitly fix model parameters or their gradients. Examples include localized changes in regularization or spatially-varying structure constraints. An example of the former is found in Booker et al. (2004) in which the authors, starting from the model in Fig. 13, locally relaxed the model structure regularization across the 410 km transition-zone, thus removing the roughness penalty for discontinuous resistivity structure across this boundary. This is motivated by seismic evidence of a change in mineralogy at this boundary, and suggests a discontinuity in resistivity is plausible. As imposed in the inversion, however, a resistivity discontinuity is not required, but simply permitted. The resulting inverse model (not shown) exhibits a strong discontinuity at the 410 km boundary to the east of the subducting slab but not to the west, stengthening the argument for an east/west change in transition-zone structure. In a different manner, the stochastic regularization of Maurer et al. (1998) uses independent geostatistical information (from well logs, ground truth, etc.) to steer an inversion toward a model with similar spatial continuity. In this fashion independent information is

incorporated into inversion without explicitly defining model structure. This approach does not, however, treat the two sets of information on equal footing, as the results of one analysis are used as fact to constrain the other analysis. This is often a reasonable approach, as the level of certainty in information can vary greatly. In other cases, an analysis giving equal treatment to both sets of information is more appropriate.

4.2.4 Constrained Multi-property Inversion and Structure Classification

CMPI and structure classification treat independent sources of information on equal footing during inversion, or post-inversion, respectively. CMPI provides the means by which to steer or regularize two or more independent data sets by taking advantage of theoretical, empirical, or model structural linkages between the data, physical properties, or models. CMPI is most commonly applied to geophysical methods characterized by non-unique inverse problems. In allowing for interaction between the data or models, the subspace of models which fit a given data set (in a misfit sense) is reduced to those acceptable to multiple data sets (Fig. 16).

Both CMPI and structure classification can compensate for variations in the resolution of individual techniques. Take the example of combining magnetotellurics with seismic refraction; magnetotellurics typically has superior lateral resolution, and thus may be sensitive to a vertical boundary that is consistent with, though invisible to the refraction data. CMPI will produce a vertical boundary in the resulting velocity model if tied in some manner to the magnetotelluric data or resistivity model. This can be seen in the cross-gradient inversion in Fig. 18, in which the combined inversion more accurately recovered the vertical velocity boundaries of features E and F when inverted together with the magnetotelluric data.

CMPI is based on the same principle that drives the structural classification approach presented earlier: though the underlying physics may differ, the subsurface distribution of multiple independent physical properties arises from a common structural section. CMPI formulations differ in how they handle data incompatible with this assumption. Theoretical or empirical linkages between physical parameters result in models containing the sum, or union, of structures required by each data set. Assuming a uniform error distribution, a sharp boundary that is strongly required by one data set, and incompatible with another will result in physical property models with a diffuse boundary, fitting neither data set and splitting the misfit. In contrast, a structural linkage, such as the cross-gradient approach, allows for incompatible data, resulting in inverse models containing the intersection of features required by both data sets, yet preserving those required by a single data set in the corresponding physical property model.

4.3 Time and Scale Limitations

The mosaic of earth structure reflects an integrated history of plate tectonics on a range of scales. Tectonic studies seek to reconstruct regional development and evolution, despite missing pieces (erosion), structural overprinting and a limited view of the subsurface. Just as the extrapolation of surface geological constraints to depth is fraught with danger, the interpretation of geophysical data in the absence of geological constraints is likewise hazardous.

We are often looking at physical properties that reflect different snapshots in time. Studies in stable cratons reveal geophysical anomalies formed in the Archean that remain

to the present. When looking at active tectonic zones, the tendency is to associate subsurface geophysical structure (which cannot be dated) with the current or most recent activity. It is known, however, that faults reactivate, and that tectonic plates often deform along pre-existing zones of lithospheric weakness. A combined interpretation must take care that observations are temporily linked. Surface heat flow, for example, reflects current or recent tectonism.[13] Seismic reflections, on the other hand, such as those observed beneath the Tibetan and Altiplano Plateaus, likely reflect the current plate convergence, though they could represent much older structure, as reflections are routinely preserved in Archean crust.

The time-scale of earth processes is likewise important. A classic example is the comparison of geologic and geodetic slip rates for faults. Fault strain varies both on short time scales (within an earthquake cycle) and on long time scales (variations in tectonic stress). Geologic slip rates typically average over many earthquake cycles while geodetic slip rates reflect a fraction of an earthquake cycle. Thus disagreement is not unexpected between these different measurements. Similarly, the spatial distribution of seismicity is different for an aftershock sequence as compared to background regional seismicity. Such variations must be considered when combining seismicity with independent information.

Differences in length scale are likewise important during integration. The laboratory scale does not always translate to the field scale. The effects of weathering, chemical alteration, and heterogeneity on physical properties are not easily measured in the laboratory, in particular on the scales that many geophysical surveys average over. Though conductivity is an intensive property, field measurements of it have a defined scale. For lab samples this may be on the order of millimeters to centimeters, but for lithospheric magnetotelluric studies may reflect hundreds of kilometers. Issues of scaling manifest themselves under a range of scenarios. The study by Unsworth et al. (2005) extrapolated the viscosity reduction of partially-molten samples measured in the lab at strain rates of 10^{-5} to the mid-crust of the Tibetan Plateau, where strain rates are closer to 10^{-15}. The scaling of physical processes must therefore be carefully examined when combining lab and field measurements.

5 Conclusions

Magnetotellurics, in combination with independent geological and geophysical information offers insight into earth structure, physical state, and processes. This review highlighted some of the ways in which this combination can be carried out, and the types of information that can be gleaned from it. A range of case studies were presented in which the combination of magnetotellurics with other geophysical and geological information was crucial to constraining structure and geometry, determining physical, thermal, and compositional state, and understanding a range of earth processes. Quantitative methods, including statistical methods for structure classification and several approaches to constrained, multi-property inversion were also described.

The non-uniqueness of geophysical inverse problems requires careful consideration of assumptions and limitations. The inclusion of independent information during an inversion can be approached on several different levels which vary both in the type of constraints they place on the inversion process and the assumed certainty of the applied constraints.

[13] Anomalous heat flow due to tectonic activity typically remains for $\sim$10 Ma following the cessation of activity.

These translate into how questions and hypotheses are fomulated, and what the various outcomes imply. Finally, when integrating diverse data sets, attention must be given to issues of time and scale, as the subsurface records an incomplete and integrated earth history of diverse and sometimes unrelated events.

Acknowledgments I wish to thank the organizing committee for the 18th EM Induction Workshop for the opportunity to prepare this review. I would like to also thank those within the EM community who have drawn my attention to a range of studies. Special thanks to Kavita Jeerage for helpful discussions of mechanisms of subsurface conductivity. This review has benefited greatly from reviews by Phil Wannamaker, Mike Friedel, Stephen Box, Seth Haines, and an anonymous reviewer. Guest editors John Weaver and Pilar Queralt are thanked for guiding this manuscript to publication in a timely fashion.

References

Abraham AC, Francis D, Polvé M (2001) Recent alkaline basalts as probes of the lithospheric mantle roots of the Northern Canadian Cordillera. Chem Geol 175:361–386

Ádám A (2005) Graphite/graphitic rocks as cause of the electric conductivity anomaly and their relationship to the tectonics – a review. Acta Geod Geoph Hung 40:391–411

Ague J, Park J, Rye DM (1998) Regional metamorphic dehydration and seismic hazard. Geophys Res Lett 25:4221–4224

Allmendinger RW, Gubbels T (1996) Pure and simple shear plateau uplift, Altiplano-Puna, Argentina and Bolivia. Tectonophysics 259:1–13

Almeida E, Monteiro Santos F, Mateus A, Heise W, Pous J (2005) Magnetotelluric measurements in SW Iberia: new data for the Variscan crustal structures. Geophys Res Lett 32, doi:10.1029/2005GL022596

Alsdorf D, Nelson D (1999) Tibetan satellite magnetic low: evidence for widespread melt in the Tibetan crust? Geology 27:943–946

Aprea C, Unsworth M, Booker J (1998) Resistivity structure of the Olympic Mountains and Puget Lowlands. Geophys Res Lett 25:109–112

Archie GE (1942) The electrical resistivity log as an aid in determining some reservoir characteristics. Trans Am Inst Min Metall Pet Eng 146:54–62

Argand E (1924) La tectonique de l'Asie. Int Geol Congr Rep Sess 13:170–373

Arzate JA, Mareschal M, Livelybrooks D (1995) Electrical image of the subducting Cocos plate from magnetotelluric observations. Geology 23:703–706

Aster RC, Borchers B, Thurber C (2005) Parameter estimation and inverse problems. Elsevier Academic Press, Burlington

Baba K, Chave AD, Evans RL, Hirth G, Mackie RL (2006) Mantle dynamics beneath the East Pacific Rise at 17°S: insights from the mantle electromagnetic and tomography (MELT) experiment. J Geophys Res 111, doi:10.1029/2004JB003598

Bailey RC (1990) Trapping of aqueous fluids in the deep crust. Geophys Res Lett17:1129–1132

Bauer K, Schulze A, Ryberg T, Sobolev SV, Weber MH (2003) Classification of lithology from seismic tomography: a case study from the Messum igneous complex, Namibia. J Geophys Res 108, doi:10.1029/2001JB001073

Beaumont C, Jamieson RA, Nguyen MH, Lee B (2001) Himalayan tectonics explained by extrusion of a low-viscosity crustal channel. Nature 414:738–742

Bedrosian PA, Unsworth MJ, Fei W (2001) Structure of the Altyn Tagh Fault and Daxue Shan from magnetotelluric surveys: implications for faulting associated with the rise of the Tibetan Plateau. Tectonics 20:474–486

Bedrosian PA, Unsworth MJ, Egbert G (2002) Magnetotelluric imaging of the creeping segment of the San Andreas Fault near Hollister. Geophys Res Lett 29, doi:10.1029/2001GL014119

Bedrosian P, Unsworth M, Egbert G, Thurber C (2004) Geophysical images of the creeping San Andreas Fault: implications for the role of crustal fluids in the earthquake process. Tectonophysics 358, doi:10.1016/j.tecto.2004.02.010

Bedrosian PA, Maercklin N, Weckmann U, Bartov Y, Ryberg T, Ritter O (2007) Lithology-derived structure classification from the joint interpretation of magnetotelluric and seismic models. Geophys J Int, doi:10.1111/j.1365-246X.2007.03440.x

Bercovici D, Karato S (2003) Whole mantle convection and the transition-zone water filter. Nature 425:39–43

Bevington PR, Robinson DK (1992) Data reduction and error analysis for the physical sciences. McGraw-Hill Book Company, New York
Boerner DE, Kurtz RD, Craven JA (1996) Electrical conductivity and Paleo-Proterozoic foredeeps. J Geophys Res 101:13775–13791
Booker JR, Favetto A, Pomposiello MC (2004) Low electrical resistivity associated with plunging of the Nazca flat slab beneath Argentina. Nature 429:399–403
Borevsky L, Milanovsky S, Yakovlev L (1995) Fluid-thermal regime in the crust – superdeep drilling data. In: Barbier E, Frye G, Iglesias E, Palmason G (eds) Proceedings of the World Geothermal Congress. International Geothermal Association, Auckland, pp 975–981
Bosch M (1999) Lithology tomography: from plural geophysical data to lithology estimation. J Geophys Res 104:749–766
Bosch M, Zamora M, Utama W (2002) Lithology discrimination from physical rock properties. Geophysics 67:573–581
Brasse H, Laezaeta P, Rath V, Schwalenberg K, Soyer W, Haak V (2002) The Bolivian Altiplano conductivity anomaly. J Geophys Res 107, doi:10.1029/2001JB000391
Bruhn D, Siegfried R, Schilling F (2004) Electrical resistivity of dehydrating serpentinite. Paper presented at the tectonophysics session of the American Geophysical Union, San Francisco, 13–17 December 2004
Burnham CW (1997) Magmas and hydrothermal fluids. In: Barnes HL (ed) Geochemistry of hydrothermal ore deposits, vol 63. John Wiley, New York, p 123
Cagniard L (1953) Basic theory of the magnetotelluric method of geophysical prospecting. Geophysics 18:605–635
Christensen NI, Mooney WD (1995) Seismic velocity structure and composition of the continental crust: a global view. J Geophys Res 100:9761–9788
Clark M, Royden L (2000) Topographic ooze: building the eastern margin of Tibet by lower crustal flow. Geology 28:703–706
Cook FA, Jones AG (1995) Seismic reflections and electrical conductivity: a case of Holmes's curious dog? Geology 23:141–144
Crawford WC, Webb SC (2002) Variations in the distribution of magma in the lower crust and at the Moho beneath the East Pacific Rise at 9°–10 °N. Earth Plan Sci Let 203:117–130
Crawford WC, Webb SC, Hildebrand JA (1999) Constraints on melt in the lower crust and Moho at the East Pacific Rise, 9°48′ N, using seafloor compliance measurements. J Geophys Res 104:2923–2939
de Groot-Hedlin C, Constable S (1990) Occam's inversion to generate smooth, two-dimensional models for magnetotelluric data. Geophysics 55:1613–1624
Dell'Aversana P (2001) Integration of seismic, MT, and gravity data in a thrust belt interpretation. First Break 19:335–341
Dewey J, Burke K (1973) Tibetan, Variscan and Precambrian reactivation: product of continental collision. J Geol 81:683–692
Dietrich CR, Newsam GN (1997) Fast and exact simulation of stationary Gaussian processes through circulant embedding of the covariance matrix. SIAM J Sci Comput 18:1088–1107
Dunn RA, Toomey DR, Solomon SC (2000) Three-dimensional seismic structure and physical properties of the crust and shallow mantle beneath the East Pacific Rise at 9°30′ N. J Geophys Res 105:23,537–23,555
Emmermann R, Lauterjung J (1997) the German Continental Deep Drilling Program KTB: overview and major results. J Geophys Res 102:18,179–18,201
England PC, Houseman GA (1989) Extension during continental convergence, with application to the Tibetan Plateau. J Geophys Res 94:17,561–17,579
Evans RL, Hirth G, Baba K, Forsyth D, Mackie R (2005) Geophysical evidence from the MELT area for compositional controls on oceanic plates. Nature 437, doi:10.1038/nature04014
Falgàs E, Ledo J, Benjumea B, Marcuello A, Queralt P, Teixidó T (2006) AMT and seismic assessment of a deltaic aquifer system. Paper presented at the 18th International Workshop on Electromagnetic Induction in the Earth, El Vendrell, Spain 17–23 Spain 2006
Finn C (1990) Geophysical constraints on Washington convergent margin structure. J Geophys Res 95:19,533–19,546
Fischer MA, Nokleberg WJ, Ratchkovski NA, Pellerin L, Glen JM, Brocher TM, Booker J (2004) Geophysical investigation of the Denali fault and Alaska Range orogen within the aftershock zone of the October–November 2002, M = 7.9 Denali fault earthquake. Geology 32, doi:10.1130/G20127.1
Francheteau J, Jaupart C, Shen XJ, Kang WH, Lee DL, Bai JC, Wei HP, Deng HY (1984) High heat flow in Southern Tibet. Nature 307:32–36
Gallardo L, Meju M (2007) Joint two-dimensional cross-gradient imaging of magnetotelluric and seismic traveltime data for structural and lithological classification. Geophys J Int, doi:10.1111/j.1365-246X.2007.03366.x

Gardner GHF, Gardner LW, Gregory AR (1974) Formation velocity and density: the diagnostic basics for stratigraphic traps. Geophysics 39:770–780
Glover PWJ, Vine FJ (1995) Beyond KTB-Electrical conductivity of the deep continental crust. Surv Geophys 16:5–36
Gough DI (1986) Seismic reflectors, conductivity, water and stress in the continental crust. Nature 323: 143–144
Grapes RH (1995) Uplift and exhumation of Alpine Schist, Southern Alps, New Zealand: thermobarometric constraints. NZ J Geol Geophys 38:525–534
Guéguen Y, Palciauskas V (1994) Introduction to the physics of rocks. Princeton University Press, New Jersey
Haak V, Hutton VRS (1986) Electrical resistivity in continental lower crust. In: Dawson JB (ed) The nature of the lower continental crust, vol 23. Geological Society, Special Publication, London, pp 35–49
Haber E, Oldenburg D (1997) Joint inversion: a structural approach. Inverse Problems 13:63–77
Haberland C, Rietbrock A (2001) Attenuation tomography in the western central Andes: a detailed insight into the structure of a magmatic arc. J Geophys Res 106:11151–11167
Haberland C, Rietbrock A, Schurr B, Brasse H (2003) Coincident anomalies of seismic attenuation and electrical resistivity beneath the southern Bolivian Altiplano plateau. Geophys Res Lett 30, doi:10.1029/2003GL017492
Hamza VM, Muñoz M (1996) Heat flow map of South America. Geothermics 25:599–646
Hashin J, Shtrikman S (1962) A variational approach to the theory of effective magnetic permeability of multiphase materials. J Appl Phys 33:3125–3131
Heinson GS, Direen NG, Gill RM (2006) Magnetotelluric evidence for a deep-crustal mineralizing system beneath the Olympic Dam iron oxide copper-gold deposit, southern Australia. Geology 34:573–576
Henry S, Pollack H (1988) Terrestrial heat flow above the Andean subduction zone in Bolivia and Peru. J Geophys Res 93:15,153–15,162
Hermance JF (1979) The electrical conductivity of materials containing partial melt: a simple model from Archie's law. Geophys Res Lett 6:613–616
Höppner F, Klawonn F, Kruse R, Runkler T (1999) Fuzzy cluster analysis: methods for classification, data analysis and image recognition. John Wiley & Sons, Inc
Hoffmann-Rothe A, Ritter O, Janssen C (2004) Correlation of electrical conductivity and structural damage at a major strike-slip fault in northern Chile. J Geophys Res, doi:10.1029/2004JB003030
Hoversten GM, Constable SC, Morrison HF (2000) Marine magnetotellurics for base-of-salt mapping: Gulf of Mexico field test at the Gemini structure. Geophysics 65:1476–1488
Hyndman RD, Hyndman DW (1968) Water saturation and high electrical conductivity in the lower continental lower crust. Earth Planet Sci Lett 4:427–432
Hyndman RD, Shearer PM (1989) Water in the lower continental crust: modelling magnetotelluric and seismic reflection results. Geophys J Int 98:343–365
Hyndman DW, Harris JM, Gorelick SM (1994) Coupled seismic and tracer test inversion for aquifer property characterization. Water Resour Res 30:1965–1977
Irifune T, Ringwood AE (1987) Phase transformations in primitive MORB and pyrolite compositions to 25 GPa and some geophysical implications. In: Manghnani MH, Syono Y (eds) High-pressure research in mineral physics. Am Geophys Union Geophys Monograph, vol 39, pp 231–242
Jiracek GR, Haak V, Olsen KH (1995) Practical magnetotellurics in a continental rift environment. In: Olsen KH (ed) Continental rifts: evolution, structure, tectonics. Developments in geotechtonics, vol 25. Elsevier Press, Amsterdam, pp 103–129
Jödicke H (1992) Water and graphite in the earth's crust – an approach to interpretation of conductivity models. Surv Geophys 13:381–407
Jones AG (1987) MT and reflection: an essential combination. Geophys J R Astr Soc 89:7–18
Jones AG (1992) Electrical conductivity of the continental lower crust. In: Fountain DM, Arculus RJ, Kay RW (eds) Continental lower crust. Elsevier Press, Amsterdam
Jones AG (1998) Waves of the future: superior inferences from collocated seismic and electromagnetic experiments. Tectonophysics 286:273–298
Jones AG (1999) Imaging the continental upper mantle using electromagnetic methods. Lithos 48:57–80
Karato S (1990) The role of hydrogen in the electrical conductivity of the upper mantle. Nature 347: 272–273
Kariya KA, Shankland TJ (1983) Electrical conductivity of dry lower crustal rocks. Geophysics 48:52–61
Keller (1987) Resistivity characteristics of geological targets. In: Naibighian M (ed) Electromagnetic methods in applied geophysics. Society of Exploration Geophysicists, Tulsa Oklahoma, pp 13–51
Key K, Constable S (2002) Broadband marine MT exploration of the East Pacific Rise at 9°50′ N. Geophys Res Lett 29, doi:10.1029/2002GL016035

Key K, Constable SC, Weiss CJ (2006) Mapping 3D salt using the 2D marine magnetotelluric method: case study from Gemini Prospect, Gulf of Mexico. Geophysics 71:B17–B27
Kind R et al (1996) Evidence from earthquake data for a partially molten crustal layer in Southern Tibet. Science 274:1692–1694
Klotz J (2000) Geodätische Untersuchungen zur Deformation aktiver Kontinentalränder. Habilitationsschrift, Fachbereich Geowissenschaften, Technical University, Berlin
Kremenetsky AA, Ovchinnikov LN (1986) The Precambrian continental crust: its structure, composition, and evolution as revealed by deep drilling in the USSR. Precambrian Res 33:11–43
Kurtz RD, DeLaurier JM, Gupta JC (1986) A magnetotelluric sounding across Vancouver Island detects the subducting Juan de Fuca plate. Nature 321:596–599
Lanczos C (1997) Linear differential operators. Dover Publications, Mineola
Lebedev EB, Khitarov NI (1964) Dependence on the beginning of melting of granite and the electrical conductivity of its melt on high water vapor pressure. Geochem Int 1:193–197
Ledo J, Jones AG (2005) Upper mantle temperature determined from combining mineral composition, electrical conductivity laboratory studies and magnetotelluric field observations: application to the intermontane belt, Northern Canadian Cordillera. Earth Planet Sci Lett 236:258–268
Lemonnier C, Marquis G, Perrier F, Avouac J-P, Chitraker G, Kafle B, Gautam U, Tiware D, Bano M (1999) Electrical structure of the Himalaya of Central Nepal: high conductivity around the mid-crustal ramp along the MHT. Geophys Res Lett 26:3261–3264
Li S, Unsworth MJ, Booker JR, Wei W, Tan H, Jones AG (2003) Partial melt or aqueous fluid in the mid-crust of Southern Tibet? Constraints from INDEPTH magnetotelluric data. Geophys J Int 153:289–304
Linde N, Binley A, Tryggvason A, Pedersen LB, Revil A (2006) Improved hydrogeophysical characterization using joint inversion of cross-hole electrical resistance and ground-penetrating radar traveltime data. Water Resour Res 42, doi:10.1029/2006WR005131
Lines LR, Schultz AK, Treitel S (1988) Cooperative inversion of geophysical data. Geophysics 53:8–20
Luque FJ, Pasteris JD, Wopenka B, Rodas M, Barrenechea JF (1998) Natural fluid-deposited graphite: mineralogical characteristics and mechanisms of formation. Am J Sci 298:471–498
Makovsky Y, Klemperer SL (1999) Measuring the seismic properties of Tibetan bright spots: free aqueous fluid in the Tibetan middle crust. J Geophys Res 104:10,795–10,825
Marquardt DW (1970) Generalized inverse, ridge regression, biased linear, and nonlinear estimation. Techtonometrics 12:591–612
Marquis G, Hyndman RD (1992) Geophysical support for aqueous fluids in the deep crust: seismic and electrical relationships. Geophys J Int 110:91–105
Maurer H, Holliger K, Boerner DE (1998) Stochastic regularization: smoothness or similarity? Geophys Res Lett 25, doi:/10.1029/98GL02183
Maercklin N (2004) Seismic structure of the Arava Fault, Dead Sea Transform. PhD. thesis, University of Potsdam, Potsdam
Maercklin N, Bedrosian PA, Haberland C, Ritter O, Ryberg T, Weber M, Weckmann U (2005) Characterizing a large shear-zone with seismic and magnetotelluric methods: the case of the Dead Sea Transform. Geophys Res Lett 32, doi:10.1029/2005GL022724
MacQueen J (1967) Some methods for classification and analysis of multivariate observations. In: Proc 5th Berkeley Symp on Mathem Stat and Prob, University of California, Berkeley, 281:297
Manglik A, Verma SK (1998) Delineation of sediments below flood basalts by joint inversion of seismic and magnetotelluric data. Geophys Res Lett 25:4015–4018
Mechie J, Sobolev SV, Ratschbacher L, Babeyko AY, Bock G, Jones AG, Nelson KD, Solon KD, Brown LD, Zhao W (2004) Precise temperature estimation in the Tibetan crust from seismic detection of the α–β quartz transition. Geology 32, doi:10.1130/G20367.1
Menke W (1984) Geophysical data analysis: discrete inverse theory. Academic Press, New York
Merzer AM, Klemperer SL (1992) High electrical conductivity in a model lower crust with unconnected, conductive, seismically reflective layers. Geophys J Int 108:895–905
Métivier F, Gaudemer Y, Tapponnier P, Meyer B (1998) Northeastward growth of the Tibet Plateau deduced from balanced reconstruction of two depositional areas: the Qaidam and Hexi Corridor Basins, China. Tectonics 17:823–842
Meyer B, Tapponnier P, Boujot L, Métivier F, Gaudemer Y, Peltzer G, Shunmin G, Zhitai C (1998) Crustal thickening in Gansu-Qinghai, lithospheric mantle subduction, and oblique, strike-slip controlled growth of the Tibetan Plateau. Geophys J Int 135:1–47
Molnar P (1988) A review of geophysical constraints on the deep structure of the Tibetan Plateau, the Himalayas and the Karakorum and their tectonic implications. Philos Trans R Soc London Ser A 326:33–88

Monteiro Santos FA, Sultan SA, Represas P, El Sorady AL (2006) Joint inversion of gravity and geoelectrical data for groundwater and structural investigation: application to the northwestern part of Sinai, Egypt. Geophys J Int 165:705–718
Mosegaard K, Sambridge M (2002) Monte Carlo analysis of inverse problems. Inverse Problems 18:29–54
Mosegaard K, Tarantola A (2002) Probabilistic approach to inverse problems. In: International handbook of earthquake and engineering seismology. Academic Press, San Diego
Muñoz G, Rath V (2006) Beyond smooth inversion: the use of nullspace projection for the exploration of non-uniqueness in MT. Geophys J Int 164:301–311
Nelson KD et al (1996) Partially molten middle crust beneath Southern Tibet: synthesis of project INDEPTH results. Science 274:1684–1688
Nesbitt BE (1993) Electrical resistivities of crustal fluids. J Geophys Res 98:4301–4310
Nolasco R, Tarits P, Filloux J, Chave A (1998) Magnetotelluric imaging of the Society Islands hotspot. J Geophys Res 103:287–309
Nover G, Stoll JB, von der Gönna J (2005) Promotion of graphite formation by tectonic stress – a laboratory stress experiment. Geophys J Int 160:1059–1067
Ogawa Y, Mishina M, Goto T, Satoh H, Oshiman N, Kasaya T, Takahashi Y, Nishitani T, Sakanaka S, Uyeshima M, Takahashi Y, Honkura Y, Matsushima M (2001) Magnetotelluric imaging of fluids in intraplate earthquakes zones, NE Japan back arc. Geophys Res Lett 28:3741–3744
Orange AS (1989) Magnetotelluric exploration for hydrocarbons. Proc IEEE 77:287–317
Paasche H, Tronicke J (2007) Cooperative inversion of 2D geophysical data sets: a zonal approach based on fuzzy c-means cluster analysis. Geophysics 72:35–39
Paasche H, Tronicke J, Holliger K, Green AG, Maurer HR (2006) Interpretation of diverse physical-property models: subsurface zonation and petrophysical parameter estimation based on fuzzy c-means cluster analysis. Geophysics 71:33–44
Palacky GJ (1987) Resistivity characteristics of geological targets. In: Naibighian M (ed) Electromagnetic methods in applied geophysics. Society of Exploration Geophysicists, Tulsa, Oklahoma, pp 53–129
Park SK, Mackie RL (2000) Resistive (dry?) lower crust in an active orogen, Nanga Parbat, northern Pakistan. Tectonophysics 316:359–380
Park SK, Biasi GP, Mackie RL, Madden TR (1991) Magnetotelluric evidence for crustal suture zones bounding the southern great Valley, California. J Geophys Res 90:353–376
Park SK, Thompson SC, Rybin A, Batalev V, Bielinski R (2003) Structural constraints in neotectonic studies of thrust faults from the magnetotelluric method, Kochor Basin, Kyrgyz Republic. Tectonics 22, doi:10.1029/2001TC001318
Parker RL (1980) The inverse of electromagnetic induction: existence and construction of solutions based on incomplete data. J Geophys Res 85:4421–4428
Parker RL (1994) Geophysical inverse theory. Princeton University Press, Princeton
Parsons T, Blakely RJ, Brocher TM (2003) A simple algorithm for sequentially incorporating gravity observations in seismic traveltime tomography. In: Klemperer SL, Ernst WG (eds) The lithosphere of western North America and its geophysical characterization, vol 7. International Book Series, pp 404–417
Quist AS, Marshall WL (1968) Electrical conductivity of aqueous sodium chloride solutions from 0 to 800° and at pressures to 4000 bars. J Phys Chem 72:784–703
Raab S, Hoth P, Huenges E, Müller HJ (1998) Role of sulfur and carbon in the electrical conductivity of the middle crust. J Geophys Res 103:9681–9689
Rietbrock A, ANCORP Research Group (1999) Velocity structure and seismicity in the central Andes of northern Chile and southern Bolivia. Paper presented at the tectonophysics session of the American Geophysical Union, San Francisco, December 1999
Ritter O, Ryberg T, Weckmann U, Hofmann-Rothe A, Abueladas A, Garfunkel Z, DESERT Research Group (2003a) Geophysical images of the Dead Sea Transform in Jordan reveal an impermeable barrier for fluid flow. Geophys Res Lett 30, doi:10.1029/2003GL017541
Ritter O, Weckmann U, Vietor T, Haak V (2003b) A magnetotelluric study of the Damara Belt in Namiba: 1. Regional scale conductivity anomalies. Phys Earth Planet Int 138:71–90
Rodi W, Mackie RL (2001) Nonlinear conjugate gradients algorithm for 2-D magnetotelluric inversion. Geophysics 66:174–187
Roecker S, Thurber C, McPhee D (2004) Joint inversion of gravity and arrival time data from Parkfield: new constraints on structure and hypocenter locations near the SAFOD drill site. Geophys Res Lett 31, doi:10.1029/2003GL019396
Ross JV, Bustin RM (1990) The role of strain energy in creep graphitization of anthracite. Nature 343:58–60
Satpal O, Singh P, Sar D, Chatterjee SM, Sawai S (2006) Integrated interpretation for sub-basalt imaging in Saurashtra Basin, India. Leading Edge 25:882–885

Scales JA, Smith ML, Treitel S (2001) Geophysical inverse theory. Samizdat Press, Golden
Schalkoff R (1992) Pattern recognition: statistical, structural, and neural approaches. John Wiley and Sons, New York, 364 pp
Schilling FR, Partzsch GM, Brasse H, Schwarz G (1997) Partial melting below the magmatic arc in the central Andes deduced from geoelectromagnetic field experiments and laboratory data. Phys Earth Planet Inter 103:17–32
Schmeling H (1986) Numerical models on the influence of partial melt on elastic, anelastic, and electrical properties of rocks. Part II: electrical conductivity. Phys Earth Planet Int 43:123–136
Schwalenberg K, Rath V, Haak V (2002) Sensitivity studies applied to a 2-D resistivity model from the central Andes. Geophys J Int 150:673–686
Shankland TJ, Ander MA (1983) Electrical conductivity, temperatures, and fluids in the lower crust. J Geophys Res 88:9475–9484
Sibson RH (1994) Crustal stress, faulting and fluid flow. In: Parnell J (ed) Geofluids: origin, migration and evolution of fluids in sedimentary basins, vol 78. Geol Soc Spec Publ, London, pp 69–84
Simpson F, Bahr K (2005) Practical magnetotellurics. Cambridge University Press, Cambridge
Solon KD (2000) Electromagnetic images of the Bangong-Nujiang suture zone of central Tibet: From INDEPTH magnetotelluric data. M.S. thesis, Syracuse University, Syracuse, New York, 81 pp
Solon KD, Jones AG, Nelson KD, Unsworth MJ, Kidd WF, Wei W, Tan H, Jin S, Deng M, Booker JR, Li S, Bedrosian P (2005) Structure of the crust in the vicinity of the Bangong-Nujiang suture in central Tibet from INDEPTH magnetotelluric data. J Geophys Res 110, doi:10.1029/2003JB002405
Stesky RM, Breace WF (1973) Electrical conductivity of serpentinized rocks to 6 kilobars. J geophys Res 78:7614–7621
Symons NP, Crosson RS (1997) Seismic velocity structure of the Puget Sound region from 3D nonlinear tomography. Geophys Res Lett 24:2593–2596
Tauber S, Banks R, Ritter O, Weckmann U (2003) A high-resolution magnetotelluric survey of the Iapetus Suture Zone in southwest Scotland. Geophys J Int 153:548–568
Telford WM, Geldart LP, Sheriff RE, Keys DA (1976) Applied geophysics. Cambridge University Press, Cambridge
Thompson AB, Connelly JA (1990) Metamorphic fluids and anomalous porosities in the lower crust. Tectonophysics 182:47–55
Tikhonov AN (1950) On the determination of the electric characteristics of deep layers of the Earth's crust. Dokl Akad Nauk SSSR 73:295–297 [Reprinted in Vozoff, 1986]
Tikhonov AN, Arsenin VY (1979) Methods for solving ill-posed problems. Nauka, Moscow
Torgersen T (1990) Crustal-scale fluid transport. Eos Trans AGU 71:1–13
Tronicke J, Holliger K, Barrash W, Knoll MD (2004) Multivariate analysis of cross-hole georadar velocity and attentuation tomograms for aquifer zonation. Water Resour Res 40, doi:10.1029/2003WR002031
Tuncer V, Unsworth MJ, Sirapunvaraporn W, Craven JA (2006) Exploration for unconformity-type uranium deposits with audiomagnetotelluric data: a case study from the McArthur River mine, Saskatchewan, Canada. Geophysics 71:201–209
Tyburczy JA, Waff HS (1983) Electrical conductivity of molten basalt and andesite to 25 kbar pressure: geophysical significance and implications for charge transport and melt structure. J Geophys Res 88:2413–2430
Unsworth MJ, Malin PE, Egbert GD, Booker JR (1997) Internal structure of the San Andreas fault zone at Parkfield, California. Geology 25:359–362
Unsworth M, Bedrosian P, Eisel M, Egbert G, Siripunvaraporn W (2000a) Along strike variations in the electrical structure of the San Andreas Fault at Parkfield, California. Geophys Res Lett 27:3021–2024
Unsworth MJ, Lu X, Watts MD (2000b) CSAMT exploration at Sellafield: characterization of a potential radioactive waste disposal site. Geophysics 65:1070–1079
Unsworth MJ, Jones AG, Wei W, Marquis G, Gokarn SG, Spratt JE, INDEPTH-MT Team (2005) Crustal rheology of the Himalaya and Southern Tibet inferred from magnetotelluric data. Nature 438, doi:10.1038/nature04154
Vozoff K (ed) (1986) Magnetotelluric methods. Society of Exploration Geophysicists, Geophysical reprint series, No 5, Tulsa, Oklahoma, 763 pp
Vozoff K (1991) The magnetotelluric method. In: Naibighian M (ed) Electromagnetic methods in applied geophysics. Society of Exploration Geophysicists, Tulsa, Oklahoma
Waff HS, Weill DF (1975) Electrical conductivity of magmatic liquids: effects of temperature, oxygen fugacity, and composition. Earth Planet Sci Lett 28:254–260
Waff HE, Rygh JT, Livelybrooks DW, Clingman WW (1988) Results of a magnetotelluric transect across western Oregon: crustal resistivity structure and the subduction of the Juan de Fuca plate. Earth Planet Sci Lett 87:313–324

Walcott RI (1998) Models of oblique compression: late Cenozoic tectonics of the South Island of New Zealand. Rev Geophys 36:1–26

Wannamker PE (1986) Electrical conductivity of water-undersaturated crustal melting. J Geophys Res 91:6321–6327

Wannamaker PE (2000) Comment on "The petrologic case for a dry lower crust" by Bruce W. D. Yardley and John. W. Valley. J Geophys Res 105:6057–6064

Wannamaker PE, Doerner WM (2002) Crustal structure of the Ruby Mountains and southern Carlin Trend region, Nevada, from magnetotelluric data. Ore Geol Rev 21:185–210

Wannamaker PE, Booker JR, Jones AG, Chave AD, Filloux JH, Waff HS, Law LK (1989) Resistivity cross section through the Juan de Fuca subduction system and its tectonic implications. J Geophys Res 94:14127–14144

Wannamaker PE, Jiracek GR, Stodt JA, Caldwell TG, Gonzalez VM, McKnight JD, Porter AD (2002) Fluid generation and pathways beneath an active compressional orogen, the New Zealand Southern Alps, inferred from magnetotelluric data. J Geophys Res 107, doi:10.1029/2001JB000186

Wei W, Unsworth M, Jones A, Tan H, Nelson D, Booker J, Chen L, Li S, Solon K, Bedrosian P, Jin S, Deng M, Ledo J, Kay D, Roberts B (2001) Widespread fluids in the Tibetan Crust. Science 292:716–718

Willett SD, Beaumont C (1994) Subduction of Asian lithospheric mantle beneath Tibet inferred from models of continental collision. Nature 369:642–645

Withers R, Eggers D, Fox T, Crebs T (1994) A case study of integrated hydrocarbon exploration through basalt. Geophysics 59:1666–1679

Xiao W, Unsworth MJ (2006) Structural imaging in the Rocky Mountain foothills (Alberta) using magnetotelluric exploration. AAPG Bull 90:321–333

Xu Y, Shankland TJ (1999) Electrical conductivity of orthopyroxene and its high pressure phases. Geophys Res Lett 26:2645–2648

Xu Y, Poe BT, Shankland TJ, Rubie DC (1998) Electrical conductivity of olivine, wadsleyite and ringwoodite under upper-mantle conditions. Science 280:1415–1418

Yardley BWD (1986) Is there water in the deep continental crust? Nature 323:111

Yardley BWD, Valley JW (1997) The petrologic case for a dry lower crust. J Geophys Res 102:12173–12185

Yardley BWD, Valley JW (2000) Reply. J Geophys Res 105:6065–6068

Yuan X et al (2000) Subduction and collision processes in the central Andes constrained by converted seismic phases. Nature 408:958–961

Zelt CA (1998) Lateral velocity resolution from three-dimensional seismic refraction data. Geophys J Int135:1101–112

Zhao W, Mechie J, Brown LD, Guo J, Haines S, Hearn T, Klemperer SL, Ma YS, Meissner R, Nelson KD, Ni JF, Pananont P, Rapine R, Ross A, Saul J (2001) Crustal structure of central Tibet as derived from project INDEPTH wide-angle seismic data. Geophys J Int 145:486–498